2023

The Development of Computational Models for Melting-Solidification Applications Using the Volume-Of-Fluid Method

Brendon Cavainolo
University of Central Florida

THE DEVELOPMENT OF COMPUTATIONAL MODELS FOR MELTING-SOLIDIFICATION APPLICATIONS USING THE VOLUME-OF-FLUID METHOD

by

BRENDON ANTHONY CAVAINOLO
B.S. UNIVERSITY OF CENTRAL FLORIDA, 2021

A thesis submitted in partial fulfillment of the requirements
for the degree of Master of Sciences
in the Department of Mechanical and Aerospace Engineering
in the College of Engineering and Computer Science
at the University of Central Florida
Orlando, Florida

Spring Term
2023

ABSTRACT

Fluids-related issues in the Aerospace industry are often multiphase in scope. Numerical modeling, such as computational fluid dynamics, is used to describe these problems, as they are difficult or impossible to describe analytically. This research uses computational fluid dynamics to describe multiphase problems related to melting-solidification and particle impingement. Firstly, a numerical model was established that uses the Volume-of-Fluid method to resolve a melting/solidifying particle. This model was verified against experiments and simplified analytical models, and a mesh independence study was done to ensure the results were independent of the mesh sizing. Next, the model was applied to two separate but related problems. The Artemis program has renewed interest in lunar dust mitigation. It is proposed that lunar regolith partially melts and becomes “sticky” when coming into contact with a jet flame, like a landing rocket. The method above was applied to a lunar regolith particle to show how these “sticky” particles can adhere to surfaces. The direct resolution methodology was also applied to a melted sand particle impinging and infiltrating a yttria-stabilized zirconia thermal barrier coating, as seen in engine turbines. Sand can infiltrate the thermal barrier coating and decrease its effectiveness. The infiltration from a single particle was compared to the infiltration from a stream of melted sand. These three efforts showcase the usefulness of directly resolving small particles using the Volume-of-Fluid method.

ACKNOWLEDGEMENTS

I would like to acknowledge the National Science Foundation Graduate Research Fellowship for providing funding for my education and this research. I would also like to acknowledge the scientists at the German Aerospace Center in Cologne, Germany for allowing me to visit and conduct research using their facilities. I would like to acknowledge my labmates, who have been extremely helpful, and encourage me to continue performing great research by performing great research themselves.

TABLE OF CONTENTS

LIST OF FIGURES

LIST OF TABLES

LIST OF ACRONYMS AND ABBREVIATIONS

AIAA	American Institute of Aeronautics and Astronautics
ASME	American Society of Mechanical Engineers
CFD	Computational Fluid Dynamics
CFL	Courant-Friedrichs-Lewy Stability Condition
CMAS	Calcium-Magnesium-Alumino-Silicate
EB-PVD	Electron Beam Physical Vapor Deposition
FD	Finite-Difference
FE	Finite-Element
FV	Finite-Volume
GRD	Giordano Viscosity Model
IAC	International Astronautical Congress
Kn	Knudsen Number
LMDE	Lunar Module Descent Engine
NASA	National Aeronautics and Space Administration
N-S	Navier-Stokes
Nu	Nusselt Number
Pr	Prandtll Number
Re	Reynold's Number
SEM	Scanning Electron Microscopy
St	Stokes' Number
TBC	Thermal Barrier Coating
TEM	Transmission Electron Microscopy
VOF	Volume-of-Fluid
We	Weber Number
YSZ	Yttria-Stabilized Zirconia

CHAPTER ONE:

INTRODUCTION

Background on Computational Fluid Dynamics

This section presents an overview of the fundamental mathematics and physics concepts that are relevant to this thesis, and discusses the organization of this thesis. Computational Fluid Dynamics (CFD) is a method of solving the governing equations of fluid flow using approximate, numerical methods [2]. More specifically, the Navier-Stokes equations (shown in index form below) are simplified based on the user-defined physics of the simulation, and are approximated with a numerical approximation technique, such as finite-difference (FD), finite-volume (FV), or finite-element methods (FE). Next, the user-defined numerical scheme (usually implicit or explicit) and the numerical accuracy (usually first or second order) are employed. Then, the resulting form of the N-S equations are organized into linear systems of equations, and solved [2].

Conservation of Mass

$$\frac{\partial u_i}{\partial x_i} = 0$$

Conservation of Momentum

$$\rho\left(\frac{\partial u_i}{\partial t} + u_j\frac{\partial u_i}{\partial x_j}\right) = \rho g_i - \frac{\partial p}{\partial x_i} + \mu\frac{\partial^2 u_i}{\partial x_j^2}$$

Conservation of Energy

$$\frac{\partial T}{\partial t} + u_i\frac{\partial T}{\partial x_i} = \alpha\left(\frac{\partial T}{\partial x_i}\right) + \frac{\theta}{\rho c_p}$$

The FV method solves the integral forms of the above equations (derived from Reynold's Transport Theorem). The first step in finding a FV solution is to discretize a spatial domain into a certain number of cells, and to discretize the temporal domain into timesteps. Boundary conditions and initial conditions are used to create an initial solution on the spatial and temporal domains. At

each cell face, a wall flux is solved for (say, mass or momentum flux), this wall flux is interpolated to then solve for the flux at the cell center. This is done over and over again until a solution is reached (that is, when convergence criteria are satisfied) [2].

Time discretization techniques are often one of two categories: explicit, or implicit. Explicit discretization relies solely on information from the previous time-steo, whereas implicit discretization relies on both information from the previous timestep, and information from the next timestep [2].

Another important consideration in CFD simulations is whether to use a segregated or coupled method to solve the governing equations. The main difference between the two methods is that the coupled method combines all of the governing equations into one large linear system of equations, and solves all of the flow variables simultaneously, and employs density-based schemes. On the other hand, segregated solvers are pressure-based and solve flow variables iteratively using several different systems of equations [3].

Stability in a CFD simulation is generally characterized by Von-Neumann Stability Analysis, which essentially says that the round-off error, ϵ, must take the form $|\epsilon^{n+1}/\epsilon^{n}| \leq 1$, where n is the timestep. Round-off error is represented by an arbitrary function, and that arbitrary function is approximated using a Fourier Series expansion. The result of this analysis leads to a dimensionless number, called the Courant number, which is a function of the velocity, mesh size, and timestep. The criterion for stability is called the CFL criterion, and generally means that the Courant number must be close to unity for a solution to be stable. It is important to note that this the CFL criteria is generally necessary, but not always sufficient for a stable solution. As solvers get more complex, there are more stability criteria to consider [2].

$$Co = u\frac{\Delta t}{\Delta x} \sim 1$$

The work in this thesis relies heavily on numerical methods for multiphase flow, specifically the Eulerian approach to multiphase flow. In an Eulerian multiphase flow, each phase is modeled as continuous, as opposed to a Lagrangian approach where one or multiple phases are modeled as discrete [4]. There are several techniques used in Eulerian multiphase flow problems, and they can generally be categorized in one of two ways: surface-tracking, or volume-tracking [5]. The difference between the two methods can be seen in Figure 1. The surface-tracking method uses marker points and interpolation to track the interface, whereas in volume-tracking methods, there is no explicit market that tracks the interface, and special methods are required [5]. One such way to track the volumetric interface is through the Volume-of-Fluid (VOF) method.

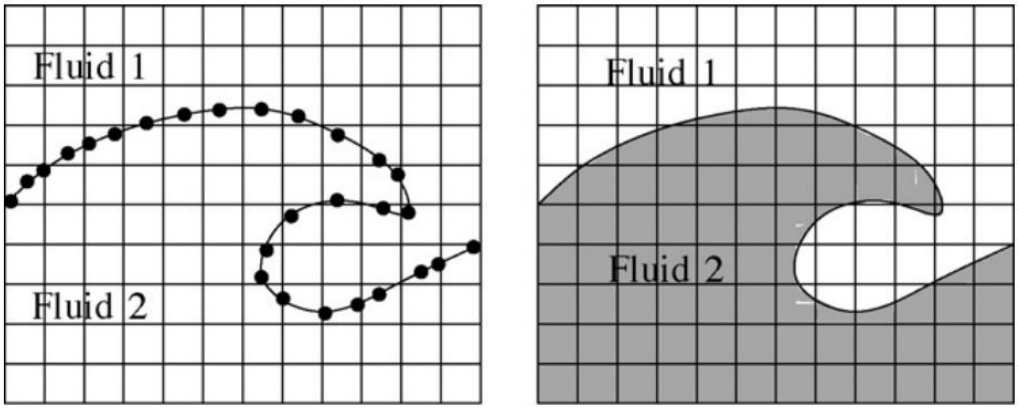

Figure 1: Difference Between Surface-tracking (left) and Volume-tracking (right) methods in Eulerian Multiphase Flow [5]

The Volume-of-Fluid (VOF) method is a volume method that obtains a single set of flow equations by volume-averaging the governing equations for each fluid. The volume-averaging can best be described in Figure 2. Then, the information for each fluid is tracked with a volume fraction

transport equation seen below [6]. Special treatment of the interface is also possible, such as including the surface tension force, where the curvature of the interface is determined and from there, another term is added to the momentum balance equations [7].

$$\frac{\partial \gamma}{\partial t} + \frac{\partial U_i \gamma}{\partial d_i} = 0$$

Issues arise in the VOF method when the above equations are discretized in certain ways. For example, the first order upwind method causes smearing at the interface because of numerical diffusion [5].

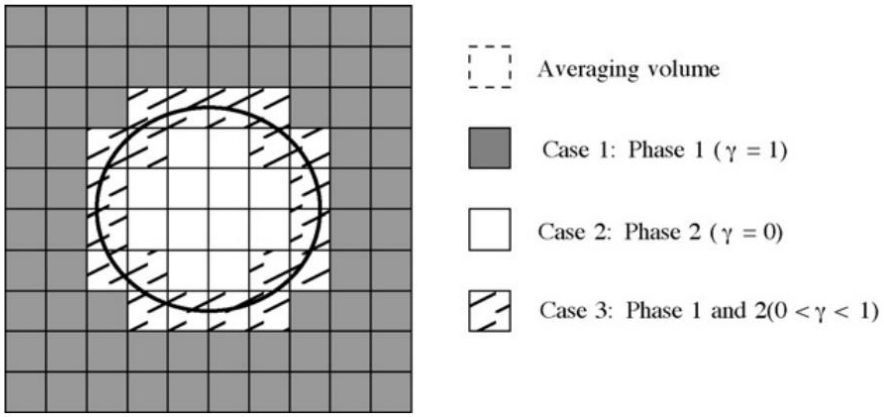

Figure 2: Cases for volume averaging in the VOF method

Background on CMAS and TBC

Calcium-Magnesium-Alumino-Silicate (CMAS) particles are a classification of particles that include sand, and volcanic ash [8]. CMAS compositions can vary greatly around the world, and thus, representative samples are often synthesized. A comparison of a sample of CMAS taken from Icelandic volcanic ash, and two synthesized variants of CMAS is shown in Table 1 [9]. Important properties, such as viscosity, vary greatly from sample to sample. However, models

exist that can predict some of these properties based on the composition, such as the GRD viscosity model [10]. Unfortunately, experiments carried out to measure the viscosity of synthesized CMAS samples shows a large discrepancy between the GRD model and experimental measurements, as seen in Figure 1 [11].

Table 1: Compositions of Synthesized (C1 & C2) and natural CMAS [9]

Mol.%	CaO	MgO	Al_2O_3	SiO_2	FeO	TiO_2	Na_2O	K_2O	Main phases	Viscosity at 1250 °C [Log Pa s]	Melting range [°C]
CMAS 1 = C1	24.7	12.4	11.1	41.7	8.7	1.6	–	–	Pyroxene + Anorthite	−0.25	1230–1250
CMAS 2 = C2	32.4	11.2	9.8	37.3	7.8	1.4	–	–	Pyroxene + Melilite	−0.69	1215–1245
Iceland VA = I	12.5	6.1	7.4	49.7	17.6	4.3	2	0.4	Amorphous	3.5	1050–1200

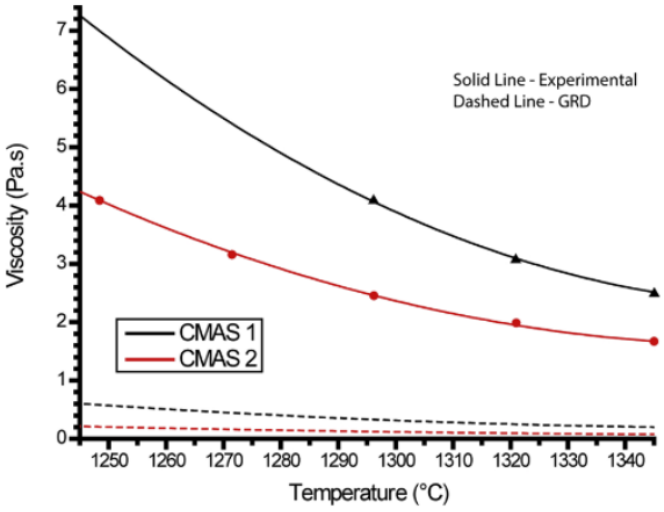

Figure 3: CMAS Viscosity comparison between experimental measurements and the GRD Model

Thermal barrier coatings are a category of high-temperature ceramic coating that are extensively used in regulating temperatures on turbine blades, especially in aircraft engines. It is critical to attain higher temperatures in these engines because higher temperatures lead to increases in efficiency [12]. A typical structure of the area around a TBC consists of the actual coating, an

oxide layer, a coat that bonds the TBC to the metallic substrate, and the metallic substrate. This structure can be seen in Figure 4 [13].

The hallmarks of an effective coating include: low thermal conductivity, phase stability, thermal shock resistance, and oxidation resistance, all of which are to protect the metallic substrate from undesirable conditions [14]. Many materials with low conductivity can be used as potential TBCs, including metals, and gemstones [15]. One of the current industry standard materials are forms of yttria-stabilized zirconia (YSZ), as it possesses greater thermal shock resistance than most other ceramics, and are stable at room temperature [16]. A disadvantage of this yttria-stabilized zirconia is that sintering, and phase changes can occur at temperatures in excess of 1200°C [17, 18].

Another important property to consider when manufacturing a TBC is the porosity. Porosity leads to lower densities, which is important because thermal conductivity and specific heat capacity are correlated to density [19]. A common method of manufacturing a popular form of YSZ, one that is 7% yttria (7YSZ), is electron beam physical vapor deposition (EB-PVD). EB-PVD produces porous 7YSZ coatings by creating a columnar microstructure in the top coat [20]. EB-PVD works by taking a target anode and hitting it with an electron beam from a charged tungsten filament. The anode is the material that the desired coating is formed from. As the beam hits the anode, the anode turns into a gaseous phase, and then solid particles precipitate from the gaseous phase onto everything in the vacuum chamber, including metallic substrates [21]. Alternatives to PVD methods include pulsed laser deposition [22], atmospheric plasma spraying [23], and chemical vapor deposition (including laser-induced) [24]. The scope of this work focuses solely on 7YSZ EB-PVD coatings.

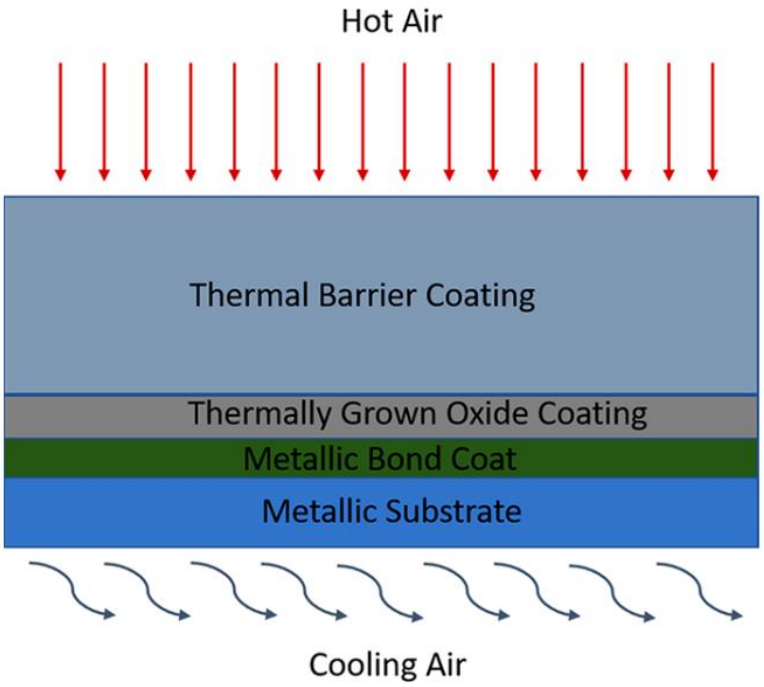

Figure 4: Typical structure of a thermal barrier coating [13]

Important properties of 7YSZ TBCs include thermal conductivity and specific heat capacity, both of which vary slightly with temperature. A graph showing thermal conductivity of various TBCs, including 7YSZ is shown in Figure 5, which shows that the thermal conductivity hovers around 1.5 W/m-K [25]. Specific heat capacity as a function of temperature for 7YSZ is shown in Figure 6, which shows a gradual increase in specific heat capacity as temperature increases [26]

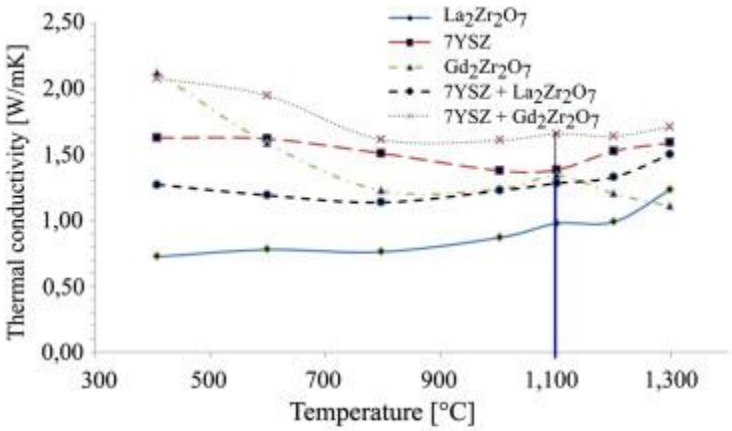

Temperature [°C]	Thermal conductivity of top coat [W/mK]				
	7YSZ	$La_2Zr_2O_7$	$Gd_2Zr_2O_7$	7YSZ + $La_2Zr_2O_7$	7YSZ + $Gd_2Zr_2O_7$
1,000	1.38	0.87	1.24	1.14	1.61
1,100	1.39	0.98	1.34	1.28	1.66
1,200	1.53	0.99	1.21	1.33	1.64
1,300	1.59	1.24	1.11	1.51	1.72

Figure 5: Thermal conductivity as a function of temperature for various TBCs [25]

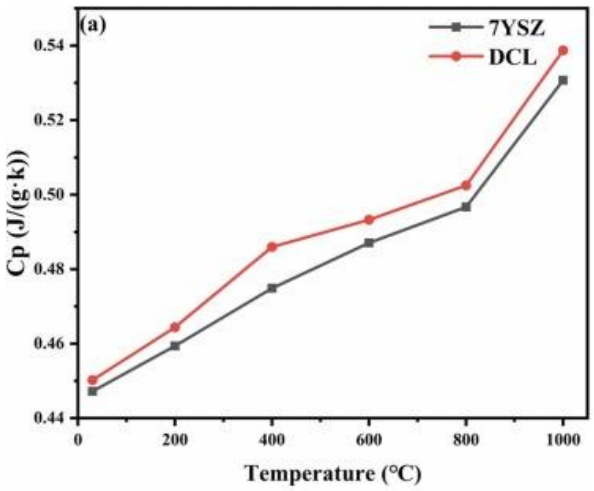

Figure 6: Specific heat capacity of several TBCs, including 7YSZ [26]

TBCs must be evaluated nondestructively during their lifecycle to ensure aircraft safety criteria are met [13]. One such test uses time-domain spectroscopy in the terahertz regime to determine surface roughness, thickness, and evolution of internal structures in the TBC [27]. The

terahertz time-domain method has also been used to determine locations of stress-induced, air-filled pores [28]. Another method uses impedance spectroscopy to measure changes in the reaction layer [29]. Other methods include ultrasonic detection [30], reflection-enhanced luminescence [31], and 3D optical topometry [32]. There are some disadvantages to these nondestructive tests, including the harmful effects of X-rays on humans [33, 34].

TBCs can experience a variety of failure mechanisms, ranging from stresses from thermal cycling [35] to the mismatch of properties between the oxide layer and other layers [36]. Another failure mechanism experienced by TBCs, and a focus of this paper, is the sintering caused by infiltration of CMAS [37]. Much of the erosion caused by CMAS in aero-engines is caused by solid CMAS particles that make it past the turbine blade [38, 39]. However, melted CMAS particles are becoming more of a problem as aero-engines achieve hotter temperature for increased efficiencies [40]. Most CMAS particles melt between 1150 – 1250 °C, depending on their composition [41-44]. However, sintering occurs when CMAS comes into contact with the TBC. In one such case, volcanic ash interacted with the YSZ TBC, and caused yttria to leach into the VA from the TBC, and form yttria iron garnet [45]. The CMAS can do this as partially or fully-melted CMAS forms deposits on top of TBCs [46].

Images such as those seen in Figure 7 [47] are achieved through scanning electron microscopy (SEM), along with sample preparation techniques such as sectioning and polishing [48]. SEM is typically used to determine the location of reaction zones and infiltration depth [49]. Transmission electron microscopy (TEM) is used to determine reaction products and phases in the oxide coating [49, 50].

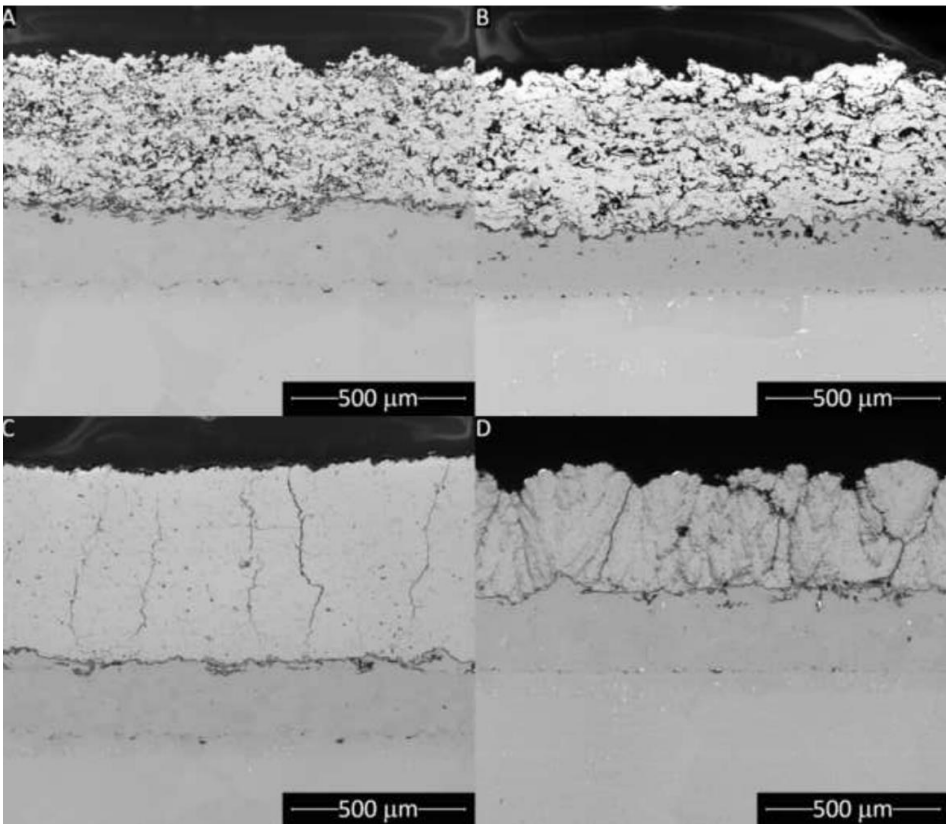

Figure 7: SEM image of an air-plasma sprayed TBC [47]

CHAPTER TWO:

DIRECTLY RESOLVED CMAS PARTICLE

This chapter is adapted from a paper published at the 2022 American Society of Mechanical Engineering Fluids Engineering Division Summer Meeting. Copyright permission was granted by the publishing organization. See following citation for more information.

Cavainolo, Brendon, and Michael Kinzel. "Investigation of Volume-of-Fluid Method to Simulate Melting-Solidification of Cmas Particles." Paper presented at the ASME 2022 Fluids Engineering Division Summer Meeting, 2022.

Introduction

The ingestion of CMAS (Calcium-Magnesium-Alumino-Silicate) particles into aircraft engines is an issue for aircraft safety and resilience. One incident occurred on British Airways Flight 9 in 1982, where all four engines on a Boeing 747 failed during flight through a cloud of volcanic ash (composed of CMAS). In this scenario, the CMAS particles melt due to high temperatures within the engine and resolidify on coolant lines [51]. This process can erode compressor blades, erode/infiltrate thermal barrier coatings, and cause overheating and stall [51]. The threat of CMAS ingestion can also take a financial toll on the commercial aviation industry. For example, the eruption of Eyjafjallajökull in Iceland caused the closure of European airspace for six days, and estimates say the closures cost commercial airlines around $1.7 billion [52]. The potential damage to aircraft and the world economy makes it imperative to understand how CMAS behaves inside aircraft engines.

This work seeks to do the following: 1) Give an overview of necessary background information to understand the processes involved in simulating CMAS, 2) Provide details of methodology in which meling-solidification of CMAS particles is directly resolved, 3) validate the previously mentioned approach using experimental correlations, theoretical values, and mesh studies, 4) Extracting transient information from the resolved CMAS particle, including temperature ratios, non-dimensional numbers, and forces acting on the particle.

Background

Melting and solidification in the context of CMAS particles demands a number of relevant dimensionless parameters. In droplet physics, the Weber number (We) is often used to predict the breakup mechanism of a droplet. The We is defined as the ratio of the inertial forces acting on the droplet to the surface tension forces experienced by the droplet [53]. Breakup mechanisms that liquid droplets can experience include vibrational breakup, bag breakup, bag-and-stamen breakup, sheet stripping, and catastrophic breakup [53]. A summary of experimental correlations between breakup mode and Weber number is shown in Table 2 . Due to high surface tension forces, the liquid droplet observed in this study stays within the vibrational breakup regime and is unlikely to break up.

Table 2: Experimental correlations for droplet breakup mode and weber number [53]

Breakup Mode	Weber No. Range
Vibrational	We ≤ 12
Bag	12 < We ≤ 50
Bag-and-Stamen	50 < We ≤ 100
Sheet Stripping	100 < We ≤ 350
Catastrophic Breakup	350 < We

The Ohnesorge Number (Oh) is defined as the ratio of viscous forces on a droplet to the inertial and surface tension forces seen by that droplet. When the Oh is less than 0.1, is an indicator that the Weber number is an accurate predictor of the droplet's breakup mechanism [54]. Reynold's number (Re) is a widely used value in fluid mechanics that relates the viscous forces to inertial forces and has many different applications. Here, the slip Re the relevant aerodynamic parameter, which is the Re associated with the difference of velocity between the CMAS particle (v_p) and the surrounding flow field (v_g). The thermal Stokes number (St_{th}) is another parameter of interest for this study, as it will be used for validation, and is defined as the ratio of particle thermal response time to fluid response time [1]. The St_{th} is also a function of the Nusselt Number (Nu), which is the ratio of convective to conductive heat transfer across the boundary of the particle [1]. The Prandtl number (Pr) is the ratio between the momentum diffusivity to the thermal diffusivity. The equations used to determine each dimensionless parameter are summarized below.

$$We = \frac{\rho v^2 D}{\sigma}$$

$$Oh = \frac{\mu}{\sqrt{\rho \sigma D}}$$

$$Re_{slip} = \frac{\rho (v_f - v_p) D}{\mu}$$

$$St_{th} = \frac{\rho_p c_p d_p^2 u_c}{6 k_f Nu * C}$$

$$Nu = \frac{h d_p}{k_f} = 2.0 + 0.6 Re_{slip}^{0.5} Pr^{0.33}$$

$$Pr = \frac{c_p \mu}{k_f}$$

Current literature has explored several important aspects of CMAS interaction with aircraft

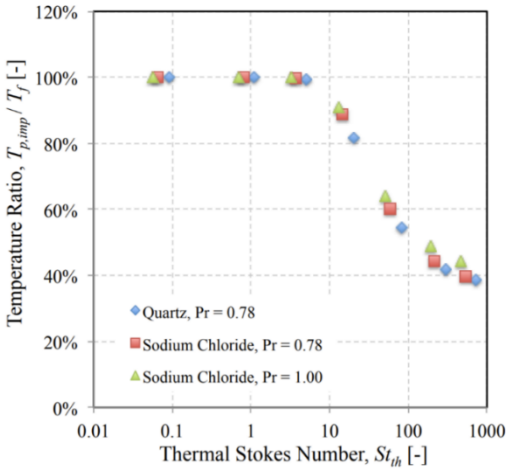

Figure 8: Validation data for temperature ratio v. Thermal stokes number [1]

engines. One such study includes a computational model exploring CMAS particle fan-blade interaction [55]. This study's goal was to find a distribution of particle sizes that are likely to make it past the fan stage of an aircraft engine [55].

Another important study investigated how the impact of CMAS particle size and chemical composition would affect the particle's time to equilibrate on the nozzle guide vane. The particle's properties were summarized using the thermal Stokes number. The ratio of particle impact temperature ($T_{p,imp}$) to the temperature of the fluid (T_f) was measured. The plot is shown in Figure 8. The plot shows that the temperature of particles with a St_{th} below unity tend to equilibrate with the temperature of the surrounding fluid in a fraction of the surrounding fluid's response time. St_{th} larger than unity led to particles that take much longer than the surrounding fluid's response time to equilibrate with the surrounding fluid. This correlation was used as validation in the results section of this paper.

Another study of interest investigated binary collision of liquid CMAS particles in conditions similar to those seen in a gas turbine [56]. This work sought to investigate CMAS particle coalescence within turbines. An important note of this study is that it also employs a direct resolution methodology to simulate CMAS. However, it does not include particle melting/solidification modeling.

Methods

The simulation of a CMAS particle was accomplished in Star-CCM+ (v.16.02.009), a commercial CFD solver from Siemens PLM Software. The particle simulation was conducted with quarter-symmetry where the domain's length was 80x larger than the particle's radius and the width and height was 20x larger than the radius. A diagram of the domain can be seen in Figure 9.

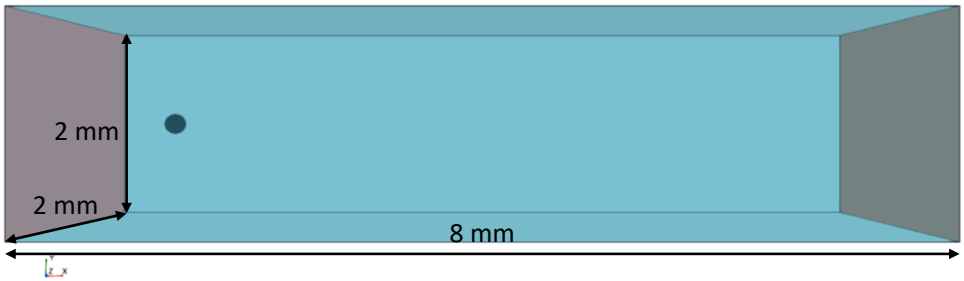

Figure 9: Shows a diagram of the domain with dimensions.

Mesh

There are several main components when it comes to meshing the particle's domain. Firstly, for the finest mesh, a trimmed-cell mesh was used where the base size was 40% of the particle's diameter (Note: this base size was changed to different sizes for the mesh study). The base size was used as the maximum cell size in the far-field. A free-surface adaptive mesh criterion

was implemented that refines the mesh in the area around the interface between the particle and the surrounding fluid. The mesh was refined to the point where the CMAS particle and it's interactions with the laminar flow are fully resolved. A diagram of the mesh can be seen in Figure 10.

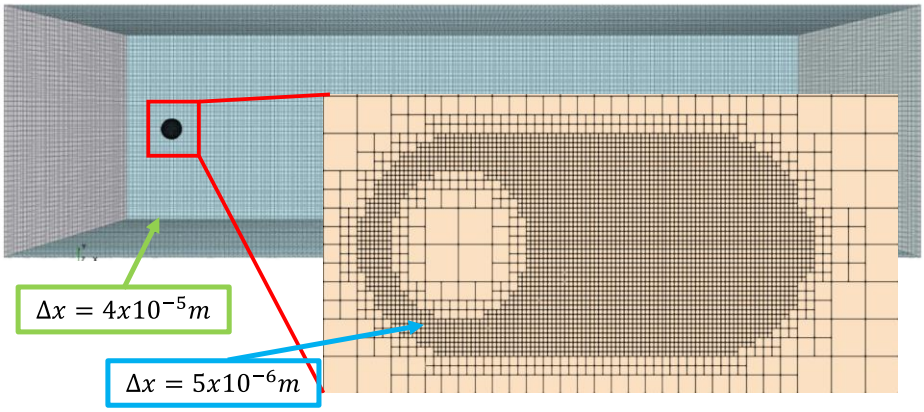

Figure 10: Shows a diagram of the mesh where the green arrow indicates the refinement of the far-field, the red square indicates the area around the droplet, and the blue arrow indiciates the refinement of the free-surface adaptive mesh

Computational Model of the Physical System

One drawback of the proposed, direct CMAS-particle-resolving method is the very small timesteps required to resolve the CMAS particle accurately. So, adaptive time-stepping combined with sub-iterations was used to ensure this happens quickly and accurately. The Courant number $\left(\frac{u\Delta t}{\Delta x}\right)$ for the adaptive-time-stepping was 1.0 and an average Courant number of around 0.5. The physical models used are also 2nd order accurate in time and space.

The particle and its domain were resolved using a laminar flow model for simplicity. Even though conditions in engines are often turbulent to promote mixing, resolving the turbulence in

the context of this study is not relevant since the main goal is to reproduce the trend seen in Figure 8.

For the multiphase physics, the Eulerian Multiphase Volume-of-Fluid method was used to simulate the interactions between the two Eulerian phases, air, and CMAS. The melting-solidification model was also enabled to quantify the degree of melting and resulting deformation of the CMAS particle. The melting-solidification model also includes a convenient flow-stop option that allows solid CMAS to be held in place while outer portions of the particle begin to melt and break off, ensuring the CMAS particle remains in the domain. Equations 7-10 show the governing equations of the Eulerian Multiphase VOF model. In these equations, the subscript i denotes a particular phase, $a_i = V_i/V$ is the volume fraction of a particular phase, and S_{a_i} is a source term defined by the initialization of the phases. Equations show the governing processes of the melting-solidification model. Here, a^*_s is the relative solid volume fraction, and $f(T^*)$ is assumed to be linear (i.e., $f(T^*) = 1 - T^*$).

Boundary Conditions

Boundary conditions are relatively simple for this study. A velocity inlet was used where the velocity was set to 100 m/s. The pressure outlet condition was used for the exit condition, and the pressure was set to ambient pressure. All other boundaries are set as symmetry planes to account for the quarter symmetry.

Benchmark and Mesh Independence Study

The validation study was conducted by fixing the particle's properties to those seen in Table 3. An important note here is that the paper whose data is being used for validation analyzes

particles with varying Pr but discovered that Pr only slightly affects the outcome. In this study, the Prandtl number is fixed. The simulation was allowed to run until the particle had fully melted. The temperature ratio described in Figure 8 was plotted against the inverse of time, making the x-axis similar to Figure 8's x-axis. The same curve was generated for 5 different mesh sizes to ensure the solution was independent of the mesh.

Gathering Results

The spatially varying properties of the CMAS particle are tracked via the center of mass of the particle. So, for example, in Re_{slip}, v_p is the velocity of the particle's center of mass. Tracking the center of mass is necessary for extracting results for this direct resolution process. Once the position data is extracted, first and second-order finite-differences are performed to construct the particle's velocity and acceleration history. From the velocity and acceleration history, the time-varying variables of interest can be calculated as well, such as Re_{slip} and drag. The particle's temperature cannot be monitored in the previously described way due to the particle not being a lumped system. Instead, both the particle's average temperature and the average temperature of an isosurface encompassing the particle are tracked. The particle length scale is the initial diameter of the particle, which, in all cases, is 100 μm. This length scale was used in calculations of Re_{slip} and We, meaning that an assumption was made that the particle's deviations from a sphere are minor throughout the time simulated. Hence, dimensionless parameters in this study assume a constant spherical shape of the particle.

Table 3: CMAS properties

Density (kg/m^3)	2690
Specific Heat (J/kg-K)	800
Thermal Conductivity (W/m-K)	92.35
Latent Heat of Fusion (J/kg-K)	144
Dynamic Viscosity (Pa-s)	11
Solidus Temperature (K)	1400
Liquidus Temperature (K)	1420
Surface Tension Coefficient (N/m)	0.4

Results And Discussion

Validation and Mesh Studies

The validation and mesh (in progress) study results are summarized in Figure 11. It is shown that the particle follows a similar pattern as in Figure 8. Figure 11 corresponds to points in Figure 8 whose St_{th} are greater than 10.

The simulations show that as the CMAS particle rises in temperature, the outer layers of the particle begin to melt. As the outer layers melt, the airflow begins to strip the liquid CMAS from the particle, and the liquid then leaves the domain at the pressure outlet. This behavior is seen in Figure 12, where the white layer surrounding the particle shows a drop in solid volume fraction, indicative of melting. The CMAS particle takes around 0.6 ms to melt in the conditions presented here, as seen in Figure 15.

A note here is that these simulations run very slowly compared to the time required for the particle to melt. Recommended timesteps from the different solvers range from 1 x 10^{-8} s to 2.5 x

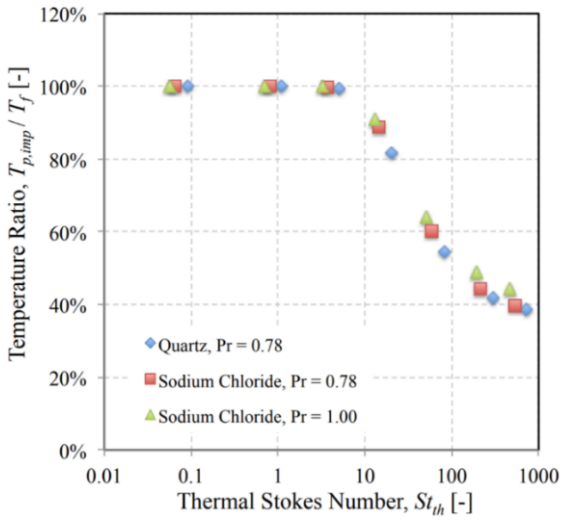

Figure 11: Validation Data For Temperature Ratio V. Thermal Stokes Number [1]

10^{-7} s, while the droplet takes around 0.6 ms to melt entirely. The simulation would need to be run for a more extended period for the particle to achieve the entire curve seen in Figure 8 (i.e., for the melted liquid particle to approach the temperature of the surrounding fluid). Some data on the curve in Figure 11 was omitted due to noise caused by temperature correction limitations in the initial timesteps of the simulation. Figure 11 also shows that the simulation has reached monotonic convergence, as the approach the converged character. It is seen that a cell size of 4 x 10^{-5} m and 5 x 10^{-5} m both show extremely similar validation curves. The 4 x 10^{-5} m case will be the one used for graphs of data proceeding Figure 11.

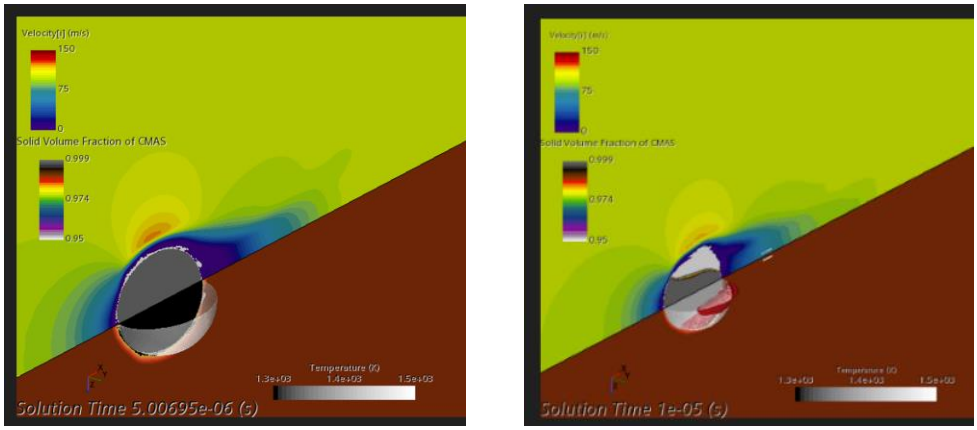

Figure 12: Shows the evolution of the CMAS particle's melting layers in the flowfield

Variables of Interest

Using the method described above, the CMAS center of mass was a starting point for gathering information about several dimensionless parameters. The Weber Number of the particle was graphed as a function of time in Figure 14. The Weber number is always lower than 12, so either no breakup or vibrational breakup [53] would occur in the particle once it has fully melted. However, it is unlikely that any breakup will occur due to the high surface tension seen in Table 3. The dimensionless parameters that depend on velocity have similarly shaped curves, as seen in Figure 13. The *Re* and *We* decrease over time because they rely on the slip velocity. Slip velocity decreases from the flow speed as the droplet accelerates after it is fully melted, causing the flow-stop condition for solid cells to disappear.

If it is assumed that drag is the only force acting on the particle, then Newton's 1st Law, along with the second-order finite-difference of position, can be used to create a drag v. time curve (Figure 16). Interestingly, the time-averaged drag value extracted from this data is 1.5268 x 10^{-6} N. A theoretical drag value calculated from Stokes' Law for drag on spheres at low *Re* is 1.706 x 10^{-6} N. Comparing these two values show only a 10% difference. The relative closeness of these

values provided confidence in the aerodynamics prediction of the direct resolution approach. Plugging in the correlation retrieved from Stokes' Law to the general equation for drag coefficient yields an approximate form of the drag coefficient for spheres at low Reynolds numbers. This correlation gives time-varying drag coefficient seen in Figure 17, and a time-averaged drag coefficient for the particle of 0.0356.

$$F_{D,Stokes} = 6\pi\mu R v_p \tag{12}$$

$$C_{d,Stokes} = \frac{F_D}{0.5\rho U^2 A} = \frac{24}{Re_{slip}} \tag{13}$$

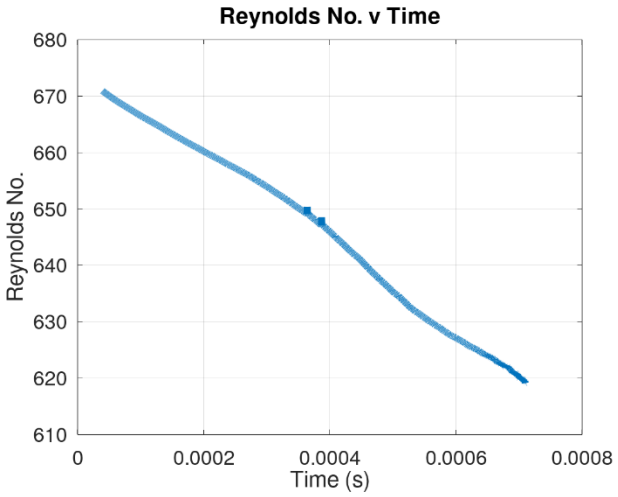

Figure 13: Shows reynold's number as a function of time

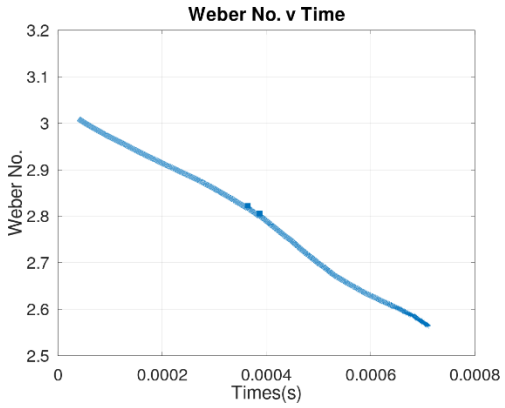

Figure 14: Shows the particle's Weber number as a function of time

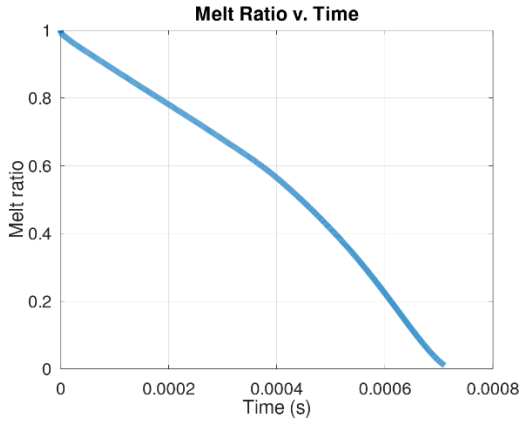

Figure 15: hows the ratio of solid cmas to the overall volume of cmas as a function of time

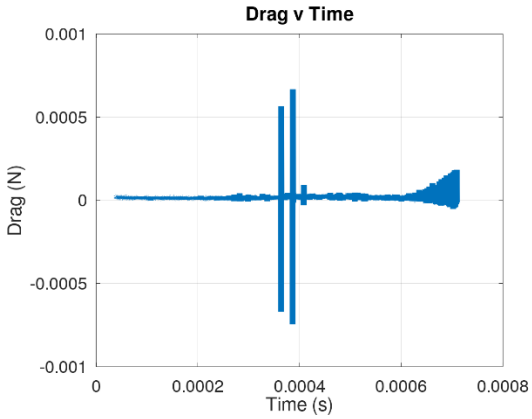

Figure 16: Shows the time-varying drag on the CMAS particle using Newton's 2nd Law.

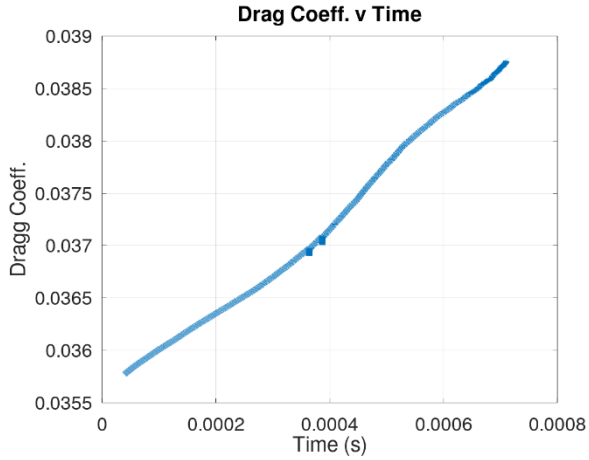

Figure 17: Shows time-varying drag coefficient of the cmas particle based on stokes' law

Conclusion

A direct resolution approach from the VOF method was used to simulate a melting CMAS particle. The resultant time-varying temperature ratio (T_p/T_g) was compared to experimental data [1] that plotted the same temperature ratio against the thermal Stokes number. This validation study shows that the direct resolution approach is valid at least for St_{th} greater than 10. Comparison to the remainder of the curve requires extended simulation runtime and a larger flow field domain. Plots of Reynold's number and Weber number were extracted from the simulation by finite-differencing the particle's center of mass's position data. Time-varying drag was also plotted in this method, and time-averaged drag compared to Stokes' Law's theoretical value. The drag comparison yielded results of similar magnitude, which further validates this method.

Future Efforts

With the direct resolution approach of simulating a melting CMAS particle developed, the method can better understand various applications. One such application is a melting CMAS particle interacting with various airfoils to understand their interactions with turbine blades. This proposed effort would involve coupling the method presented in this paper with either an Eulerian dispersed multiphase flow field or a Lagrangian phase of CMAS particles over an airfoil. Streamline data from the CMAS particles would be extracted and converted to time-varying velocity data would be fed into the direct resolution simulation. From here, particle breakup, sticking probabilities, and more can be calculated to predict the particle's interaction with the airfoil.

This method of simulating CMAS can also be used in thermal barrier coating infiltration studies, where capillary effects drive the melting CMAS into feathered microstructures. Effects of heat transfer and shear force from the droplet on the thermal barrier coating would be quantified and design recommendations could be made.

Other future efforts could include applying this method to other types of particles that experience melting, including water droplets and lunar dust particles. Similar studies to the one described above could be done for these particle types.

Lastly, the numerical methods involved in VOF melting-solidification can be moved to open-source codes, such as OpenFOAM, to allow for better pipelining between coupled simulation methods.

CHAPTER THREE: LUNAR REGOLITH MELTING, SOLIDIFICATION, AND IMPACT

The following chapter is adapted from a paper submitted to the 73rd International Astronatuical Congress. The concept of the work described here takes the now validated methodology from Chapter 4 above, and applies it to a problem that involves a lunar regolith particle encountering a plume jet, melting, and impacting a wall at a high velocity. Copyright permission was retained by the author See the citation for further information.

Cavainolo, B. A., Torres-Figueroa, A., & Kinzel, M. P. (2022). Simulating Melting-solidification of Lunar Regolith Particles Using Coupled CFD Methods.

Introduction

Lunar dust particles are problematic for many reasons. These particles have a tendency to adhere to surfaces, which can create issues from tracking particles inside habitats [57]. This property also causes particles to degrade mechanical components [58]. Mitigating the impact of lunar dust particles is going to be a challenge for future lunar exploration missions, such as the Artemis program.

This work seeks to understand dynamic and thermal properties of lunar dust particles as they interact with rocket plumes. What makes this work unique is the explicit focus on the melting-solidification of the particles, and how that melting affects the particle's interactions with other structures. Firstly, a review of the relevant literature is conducted. Then the numerical methodology is described. Next, results from the simulations are discussed. Lastly, conclusions

are made based on the results. A combination of analytical models and CFD will be used to understand this problem.

Literature Review

Methods of simulating rocket plumes in low-atmosphere environments are very well-documented, and usually involve the coupling of a Navier-Stokes based CFD solver, and a DSMC solver, such as in Figure 18.

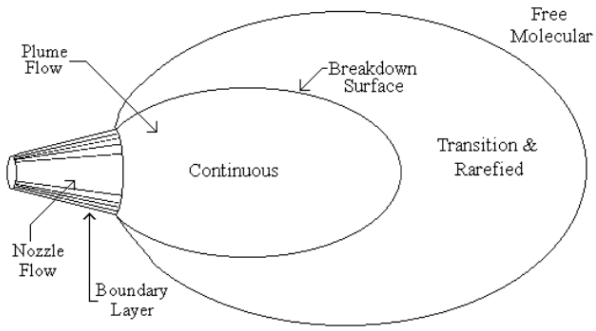

Figure 18: Description of N-S/DSMC Coupling [59]

Here, the three regions (continuous, transition/rarefied, and free molecular) can be described by their Kn. Kn is a dimensionless number defined as the ratio between a molecule's mean free path and a characteristic length scale. For a Boltzmann gas, Kn can be written as seen below.

$$Kn = \frac{k_b T}{\sqrt{2}\pi d^2 p L}$$

There are different ranges of Kn associated with different flow regimes, summarized in Table 4. In continuum flow, the assumptions of the N-S equations are valid and thus, Navier-Stokes-based CFD solvers can be used to solve for this, such as those present in commercial software such as Star-CCM+. In Slip flow, the fluid can still be treated as a continuum, but the no-slip condition is no longer valid. In transitional and free-molecular flow, the continuum assumption is no longer valid, so a different type of solver must be used. One such solver is DSMC. The DSMC method involves using probabilistic modelling to solve the Boltzmann Equation, seen below [60], where force refers to external forces on the particles, diff refers to particle diffusion, and *coll* refers to particle collisions. While commercial software often does not have DSMC solvers built-in, open-source tools, such as OpenFOAM's dsmcFoam+ [61] can be used.

$$\frac{df}{dt} = \left(\frac{\partial f}{\partial t}\right)_{\{force\}} + \left(\frac{\partial f}{\partial t}\right)_{\{diff\}} + \left(\frac{\partial f}{\partial t}\right)_{\{coll\}}$$

Table 4: Flow regimes based on Knudsen Number

Range	Regime
Kn < 0.1	Continuum Flow
0.01 < Kn < 0.1	Slip Flow
0.1 < Kn < 10	Transitional/Rarefied Flow
Kn > 10	Free-molecular Flow

For the multiphase aspect of this problem, regolith particles are often simulated using a Eulerian-Lagrangian method. In this method, particles are simulated as a dispersed phase, driven by the continuous phase. This is done because simulating a number of particles on the order of 10^7 is often not feasible from a computational resource perspective. This is especially true when the user intends to simulate particles with a distribution of diameters [62]. Lunar regolith particles exist in diameters between 0.046 mm and 0.11 mm [63], thus, a Eulerian-Lagrangian simulation strikes a better balance between realism and computational cost than an Eulerian simulation would. However, if a simulation of a single particle is desired, an Eulerian-Eulerian simulation is much more reasonable.

The Eulerian-Lagrangian multiphase method has been used for several jet plume simulations, including one in a simulated Martian environment. Here, velocity history of the Lagrangian particles were extracted to estimate the destructive impact of the regolith particles [64]. An important note for this study however is that the continuum assumption is valid on Mars, so the method was not coupled to a DSMC solver. The method was also not coupled to an Eulerian-Eulerian method that focuses on a single regolith particle.

Another study took this method one step forward by using a DSMC method to simulate the jet plume [65]. A single particle is also simulated using a Lagrangian approach with one-way coupling with the DSMC solvers [65]. An empirical correlation was used to estimate the drag force and drag coefficient on the Lagrangian particles [66] (seen below) and the dynamics of the particles were solved via Newton's 2nd Law.

$$C_D = \begin{cases} 24.0Re^{-1}, & Re < 2 \\ 18.5Re^{-1}, & 2 \leq Re < 500 \\ 0.44, & Re \geq 500 \end{cases}$$

$$F_{D,i} = m_p \frac{3\rho C_D}{4\rho_p d_p} |u_{i,t} - u_{p_i}|(u_{i,t} - u_{p_i})$$

Here, Re is given by $Re_p = \frac{\rho|u_i - u_{p_i}|d_p}{AT^\beta}$, where A and β are empirical coefficients, and T is the particle temperature [66].

The shear seen by the ground, velocity, pressure, and density fields were used to demonstrate the destructive properties of the flow field. These values were reported in terms of radial distance from the centerline of the plume, and the altitude of the lander [66]. From this work, it is seen that lighter particles (particles whose weight do not overcome the drag being exerted on the particle) experience straight line, whereas larger particles experience parabolic trajectories [66]. Smaller particles could reach speeds up to 755 m/s. Since these particles are leaving the plume region, they experience no resistance and can damage structures and instruments [66].

Another study was conducted that coupled a source flow to a DSMC solver as a replacement for simulating the continuum region [67]. This was done in the context of a flat plate in the wake of a cylinder, and to analyze the effect of non-negligible pressures in an object's wake if the object is immersed in a plume, expanding into vacuum conditions [67]. The source flow model was used to estimate boundary conditions for the DSMC solver. This was done to avoid having to simulate the high-density regions of the flow using the DSMC solver, because simulating

higher densities with DSMC is more computationally expensive. Eq. 4-8 show the equations used in the source flow model.

$$\rho(r,\theta) = \frac{2Ap_o}{V^2}\left(\frac{2}{\gamma+1}\right)^{\frac{1}{\gamma-1}}\left(\frac{r_e}{r}\right)^2 f(\theta)$$

$$f(\theta) = \cos\left(\frac{\pi\theta}{2\theta_L}\right)^{\frac{\gamma+0.41}{\gamma-1}}$$

$$\theta_L = \frac{\pi}{2}\left(\sqrt{\frac{\gamma+1}{\gamma-1}} - 1\right)$$

$$V = \sqrt{\left(\frac{2\gamma}{\gamma-1}\right)\frac{kT_0}{m}}$$

$$A = \frac{\frac{1}{2}\sqrt{\frac{\gamma-1}{\gamma+1}}}{\int_\theta^{\theta_L} \sin\theta f(\theta) d\theta}$$

Methodology

For this study, the source flow model described in Section 1.1 is employed, coupled to an Eulerian-Eulerian simulation of a single, fully-resolved lunar regolith particle.

Source Flow Model

The source flow model was written in Python 3 and applies Eq. 4-8 to a 2-dimensional grid. Where possible, the properties for the Lunar-Module Descent Engine (LMDE) were used as inputs for the source flow model [57]. These properties are summarized in Table 5.

Table 5: LMDE Properties

Property (Units)	Value
Chamber Pressure (kPa)	712.9
Nozzle Exit Temperature (K)	1533
Nozzle Exit Radius (m)	0.8001
Molecular mass (kg/mol)	3.40

From here, Eq. 7 is used to calculate a limiting velocity. The limiting velocity is essentially how fast a single molecule of gas could be travelling from the plume. An angle, θ, is calculated for every grid point relative to the position of the jet plume. θ_L is the limiting theta, or the maximum value θ can have. From here, density values can be calculated from Eq. 4 for the 2D grid. The average density on the 2D grid's outlet was calculated, and this, along with velocity data, will be used for the initial and boundary conditions for the Eulerian-Eulerian VOF simulation.

VOF Simulations

The simulation of a lunar regolith particle was accomplished in Star-CCM+ (v.16.02.009), a commercial CFD solver from Siemens PLM Software. The simulation was conducted in quarter-symmetry. The domain's length was 80x larger than the particle's radius and the width and height was 20x larger than the radius. A diagram of the domain if it was in full 3D can be seen in Figure 19. A summary of the boundary conditions is shown in

Table 6.

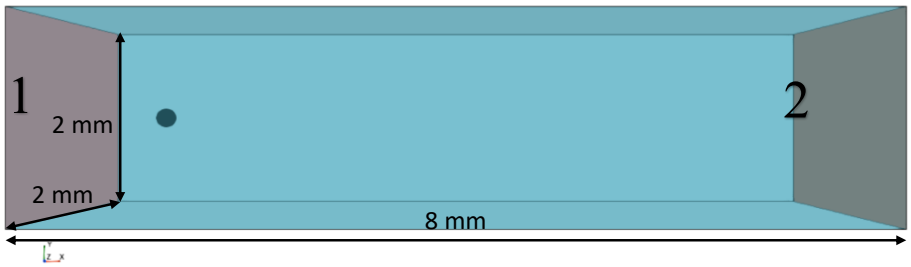

Figure 19: Example diagram of the computational domain used for the VOF simulation.

Table 6: List of Boundary Conditions

Boundary	Type	Condition
1	Velocity Inlet	1702 m/s
2	Wall	Adiabatic
Unlabeled	Pressure Outlet	455 Pa

The base size for the mesh was 40 percent of the regolith particle's diameter. This meshing size was set as the maximum cell size in the domain. From here, a free-surface adaptive mesh was used to refine the interface between the lunar regolith and the surrounding gas. The mesh was refined to the point where the regolith particle and its interactions with the laminar flow are fully resolved. A diagram of this mesh can be seen in Figure 20.

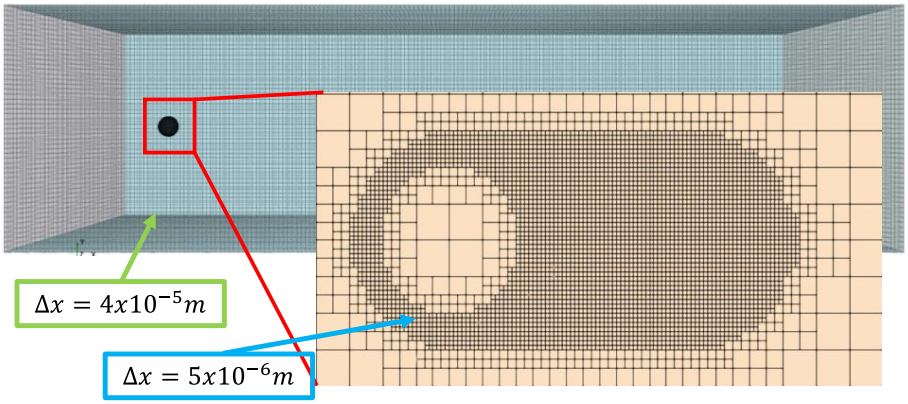

Figure 20: Example computational mesh of the domain for the regolith-particle-scale, VOF simulation

A disadvantage of this direct regolith-particle-resolving method is the very small timesteps required to resolve the regolith particle accurately. To overcome this, adaptive time-stepping and sub-iterations were used to ensure the unsteady simulation remains stable. The time-stepping was controlled by the Courant number $\left(\frac{u\Delta t}{\Delta x}\right)$, where the maximum Courant number was set to 1.0, and the average Courant number was set to 0.5. The physical models used for the simulation were 2nd order accurate in time and space.

The particle and its domain were resolved using a laminar flow model. This was done because the Re $\left(Re = \frac{\rho UL}{\mu}\right)$ is < 1000 for the flow, given the low density of gas from the source flow model.

For the multiphase physics, the Eulerian Multiphase VOF method was used to simulate the interactions between the two Eulerian phases, the lunar regolith, and the surrounding gas (N_2 in this case). A melting-solidification model was enabled to allow the particle to melt in the flow. The VOF Method for modeling, and in some cases, fully resolving multiphase flows has proven

useful in several applications. Firstly, a proof of concept application was developed, directly resolving a melting CMAS particle by validating the Thermal Stokes Number against experimental data. This showed that the VOF method can be used for these directly resolved melting-solidification cases.

Next, the same method was applied to a lunar regolith particle. This time, however, the flow was coupled to a source-flow model to account for rarefied flow conditions. Also, the melting particle experienced an impact with an adiabatic wall. Results from this study showed how a partially melted lunar regolith particle can stick to surfaces, which can be problematic for lunar missions, especially when accumulation is accounted for.

Lastly, the VOF Method was used to resolve a capillary-driven flow, the infiltration of molten CMAS into a 7YSZ EB-PVD thermal barrier coating. These simulations were characterized by the infiltration depth of the CMAS as a function of time. The simulated infiltration was several orders of magnitude faster than the experimentally measured infiltration. Possible explanations include the lack of a solidification or phase change model in the simulation, or that the modeled TBC is not sufficient for accurately resolving the infiltration. Future work here includes the addition of solidification and phase change models, and performing a similar simulation on a domain consisting of a nano-CT scan of an actual TBC.

The overall success of the models developed using the VOF Method shows its robustness at handling a wide range of multiphase flows. The VOF Method is not without its faults, however. The directly resolved CMAS particle experienced stability issues at certain mesh sizes, and had a very long run time. While the stability issues can be readily fixed by changing the mesh, the long runtime persisted through the lunar regolith and CMAS infiltration cases. Future work could

involve further optimization of the SIMPLE-C algorithm to run on GPUs, allowing faster overall runtimes.

APPENDIX A: COMMONLY USED EQUATIONS shows the governing equations that Star-CCM+ uses for the Eulerian VOF model. In these equations, the subscript i denotes a particular phase, $a_i = V_i/V$ is the volume fraction of a particular phase, and S_{a_i} is a source term defined by the initialization of the phases. Lastly, the governing processes of the melting-solidification model is decribed. Where, a^*_s is the solid volume fraction of the cell, and *f(T*)* is assumed to be linear (i.e., $f(T^*) = 1 - T^*$).

The properties of the lunar regolith that were used are based on various sources. However, where possible, the properties will be taken from a single Apollo landing site. Firstly, the thermal conductivity of Lunar Regolith has been determined to vary based on temperature [68].

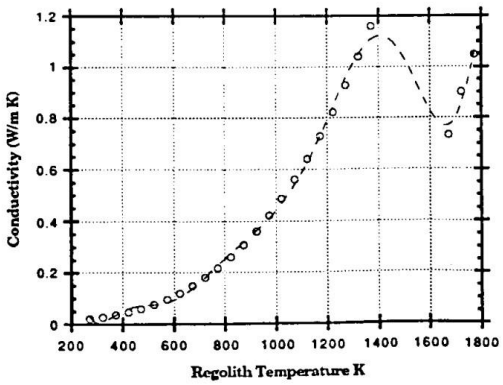

Figure 21: Thermal conductivity as a function of regolith temperature [68]

From the same study, the specific heat capacity of lunar regolith was also investigated and its relationship with temperature is shown in Figure 22 [68]. Note that these values were calculated based on a latent heat of fusion of 1429 J/kg-K [68].

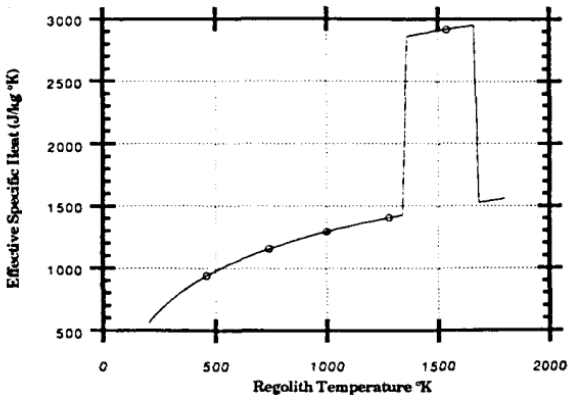

Figure 22: Specific-heat capacity for lunar regolith as a function of temperature [68].

The density of lunar regolith can vary greatly depending on soil depth, and landing site [69]. However, values generally range between 300 kg/m^3 and 2000 kg/m^3 [69].

Unfortunately, values for dynamic viscosity must come from lunar regolith simulant, rather than regolith itself. Values for regolith simulant are readily available due to the interest in using regolith to build lunar structures with additive manufacturing [70]. Viscosity values were calculated based on the shear rate, and it was found that a dynamic viscosity between 8 Pa-s and 9 Pa-s for various shear rates [70].Thus, an average value of 8.5 Pa-s will be used as the dynamic viscosity of the melted regolith.

Lastly, melting temperature is needed for the melting-solidification model. Since the regolith is a combination of several materials, the melting temperature is a range between 1373 K to 1653 K [68].

Some assumptions must be made to simplify some parts of the interface between the source flow model and the VOF simulation. Importantly, the source flow model assumes that the

temperature of the field is the same as the chamber temperature of the nozzle. So, this will have to be the starting temperature of the VOF simulation as well [67].

Results and Discussion

In this section, results from the source flow model will be shown and discussed. The implementation of the source flow model's data into the VOF model is also discussed. Lastly, data and flow visualization from the VOF model will be discusses.

The source flow model was created using a field assumed to extend 2.5 m in the +x-direction, and 0.5 m in the -y and +y directions. The 2D grid was created such that the domain was discretized into 40 points in each direction, resulting in a 40x40 grid to resolve the 2.5 m x 1.0 m domain. The results from this calculation were output in the form of two graphs, and some text data. The first graph seen in Figure 23. is a contour plot of the domain's density. The values in the graph provide sensible densities around the nozzle (at 0,0) is higher than in the far-field. The density data of interest exists here at x=2.5 m. Since the density varies radially from the nozzle, the density will take different values along x=10 m. So, the average density along the x=10m line will be used as the density for the VOF simulation.

With the average density on this boundary being ~0.017 kg/m^3, and the properties of nitrogen being known, the ideal gas law can be used to find an approximate pressure of 455 Pa. The domain of the VOF Simulation was initialized at this pressure.

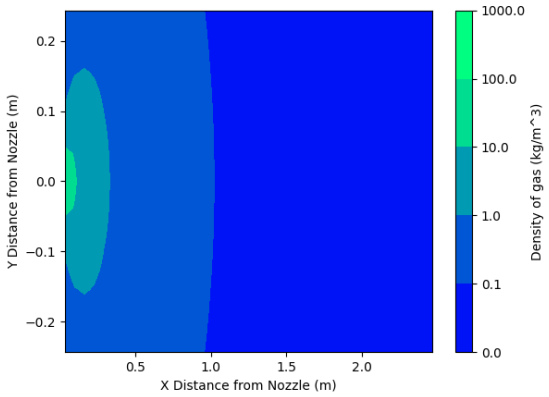

Figure 23: Contour plot of exhaust gas density. Nozzle location at (0,0).

The limiting velocity was found to be 1701 m/s from the source flow model. This velocity was used as the initial condition for the gas surrounding the regolith particle in the VOF simulation.

Figure 24 shows the initialization of the VOF domain. The solid volume fraction of the particle is tracked via a resampled volume that assigns 3D voxels to mesh cells, and colors them based on a scalar field. Since the combustion chamber temperature is between the liquidus and solidus temperatures, the particle is initialized with a solid volume fraction of around 0.36.

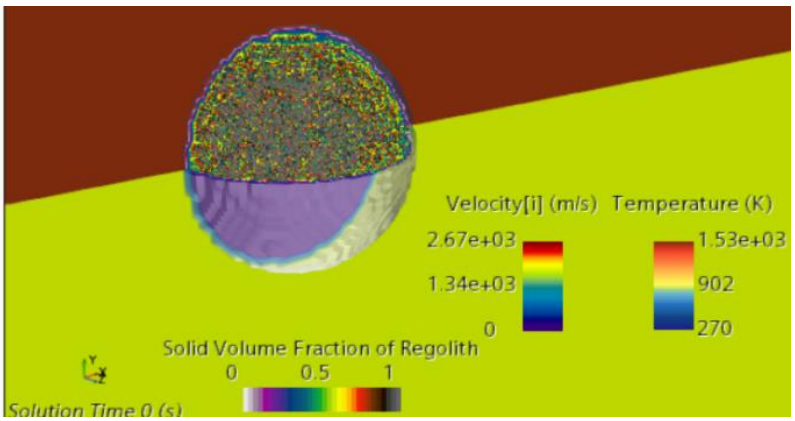

Figure 24: Visualization of the VOF initialization.

As the simulation is started, the regolith particle begins to accelerate due to the speed of the surrounding gas. The particle's temperature also begins to equilibrate with the flow. The ratio of the particle's average temperature to the average temperature of the surrounding gas is plotted in Figure 25. The temperature ratio in Figure 25 starts so high because the gas starts at a cool ambient temperature and then heats up from the boundary condition, simulating the actual temperature increase from a descent vehicle. The deformation of the regolith particle after just 5 time-steps can be seen in Figure 26. Here, the liquid outer layer of the regolith can be seen deforming around the solid core. This is important because it shows that the liquid outer layer is not entirely stripped from the particle, making it more likely to stick to surfaces.

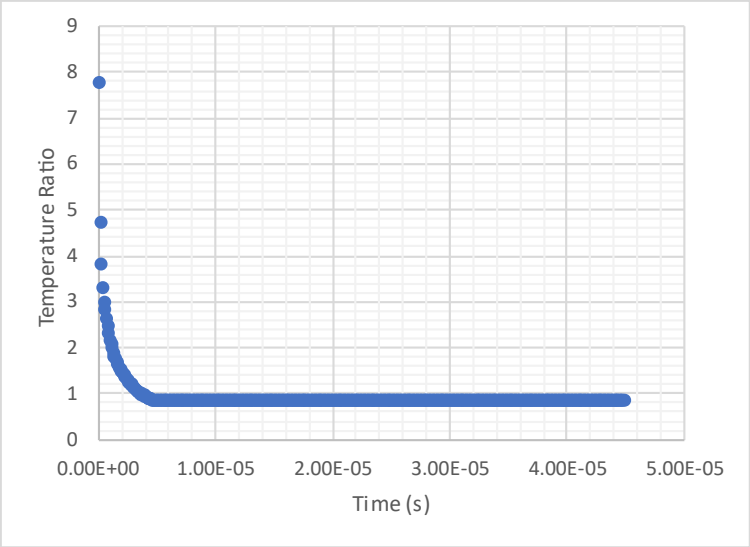

Figure 25: Plot of Temperature Ratio (i.e., Mean regolith temperature normalized by the mean gas temperature) versus time on a regolith particle.

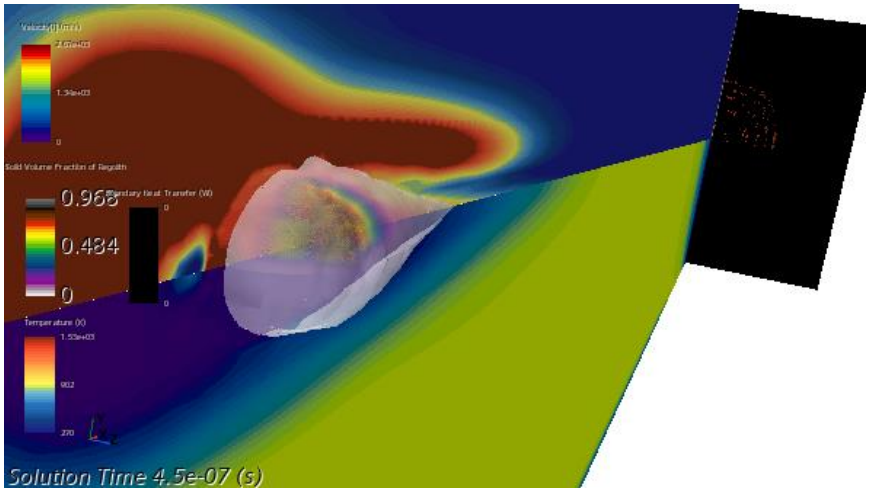

Figure 26: Visualization of regolith particle after 5 Time-steps

The ratio of the total volume of solid regolith to the total volume of regolith is also plotted against time in Figure 27. Here it can be seen that the particle remains partially liquid throughout the entire simulation, meaning that it can interact and stick to the wall at the end of the domain, rather than just bouncing off.

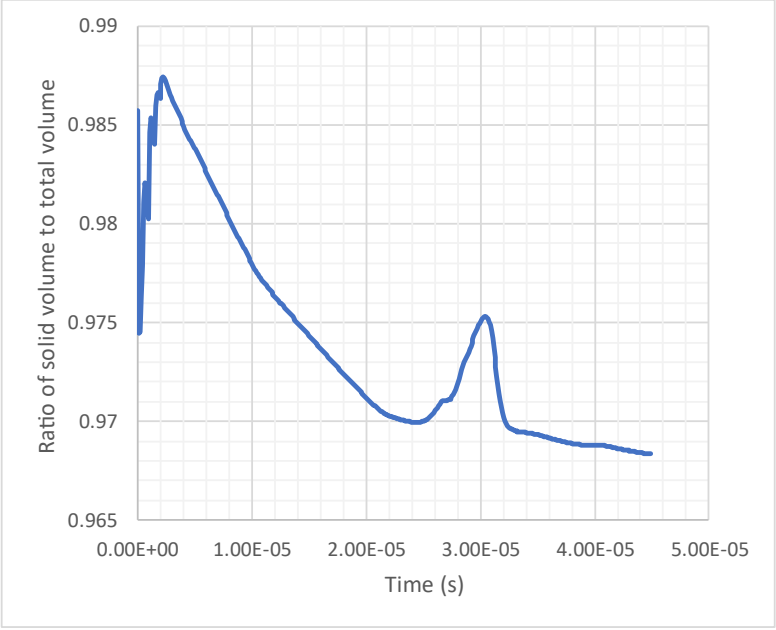

Figure 27: Ratio of solid-to-liquid volume as a function of time.

A visualization of the particle sticking to the wall is seen in Figure 28. Here, the white surface represents the outer most layer of the lunar regolith. The colors inside the white surface represent the solid volume fraction of the regolith. Lastly, the red plane represents the temperature of the gas surrounding the particle, and blue-to-yellow represents the velocity of the gas surrounding the particle. Note that this is from a head-on-collision.

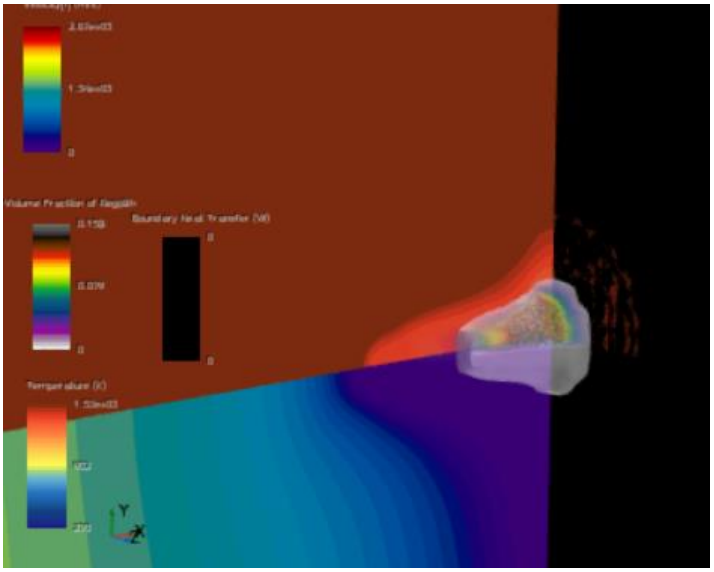

Figure 28: Visualization of Regolith Particle Sticking to Wall

From the position data of the regolith particle's center of mass shown in Figure 29, there is a correlation between the spike around 30 μs in Figure 27, and the point at which the regolith particle sticks to the wall. This finding is interesting because it shows that a wall at a lower temperature than the regolith particle will cause a sudden solidification in the regolith particle. However, as quickly as the particle resolidifies, it returns nearly to the same solid volume percentage shortly after contacting the wall. Note that this was the case if the wall was set to an adiabatic condition. That is, the wall's temperature is extracted from the interior of the domain.

Importantly though, this shows that the overall melting of the particle can be controlled by the thermal properties of the wall it contacts. Another important finding here is that if the velocity condition for the inlet is turned off, and the simulation is allowed to run ambiently after the particle has made contact with the wall, it no longer deforms or is affected significantly by gravity. This shows that the particle will not move once the engine from a descent vehicle is no longer being fired.

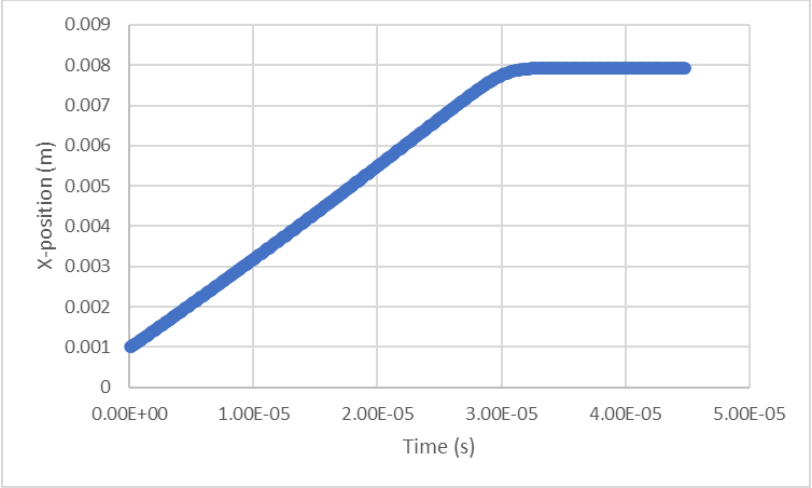

Figure 29: Position (m) vs. time (s) of regolith's center of mass

Conclusions

An understanding of the melting-solidification of lunar regolith particles between a jet plume and a structure was desired. It was hypothesized that a rocket plume causes a lunar-regolith particle to melt to a degree such that a liquid outer-layer would form around the particle. The liquid outer-layer would cause the particle to stick to surfaces and accumulate on those surfaces over time.

A source flow model was coupled to an Eulerian VOF simulation in order to model the rarefied flow experienced by the particle, and to resolve the melting-solidification of the particle, as well as it's interactions with a wall. Where possible, values relating to the LMDE were used in the source flow model, and properties of lunar regolith were taken from the same landing sites. When not possible, however, these properties were taken from different landing sites or from regolith simulant.

Results from the source flow model show low-density, high-speed flow 2.5 m away from the nozzle. These results were utilized as input conditions for the VOF simulation. The VOF simulation shows that the regolith particle initialized at the chamber temperature of the LMDE already starts off partially melted. As the flow solution is generated, the hypothesized liquid outer-layer forms around the particle and deforms. Eventually the particle hits the wall and undergoes deformation up until a certain point where it does not deform any further. The particle also undergoes a brief period of solidification as it impacts the adiabatic wall. The particle quickly returns to the stage of melting it was in before impacting the wall. However, this shows that thermal properties of the wall can impact the state of the droplet. This could potentially help create solutions for the accumulation of these particles on lunar structures.

Further work on these ideas will include particle impacts at multiple angles to see if certain angles lend themselves more to sticking or ricochet of particles. Also, different heat transfer conditions will be explored on the impacted wall to look for effective ways of mitigating particle accumulation. Some examples of different wall conditions include constant temperature, constant heat flux density, convection on external side of the wall, and then all of these conditions, but with a conduction zone inside the wall and using conjugate heat transfer.

CHAPTER FOUR: CMAS INFILTRATION OF A THERMAL BARRIER COATING

The ingestion of CMAS (Calcium-Magnesium-Alumino-Silicate) particles into aircraft engines is an issue for aircraft safety and resilience. One incident occurred on British Airways Flight 9 in 1982, where all four engines on a Boeing 747 failed during flight through a cloud of volcanic ash (composed of CMAS). In this scenario, the CMAS particles melt due to high temperatures within the engine and resolidify on coolant lines [51].This process can erode compressor blades, erode/infiltrate thermal barrier coatings, and cause overheating and stall [51]. Helicopters operating in desert climates are at an even greater risk for CMAS attack because of how often they operate in sandy conditions [71]. The threat of CMAS ingestion can also take a financial toll on the commercial aviation industry. For example, the eruption of Eyjafjallajökull in Iceland caused the closure of European airspace for six days, and estimates say the closures cost commercial airlines around $1.7 billion [52]. The potential damage to aircraft and the world economy makes it imperative to understand how CMAS behaves inside aircraft engines.

Thermal Barrier Coatings (TBCs) are ceramic coatings present in aircraft engines, usually on the high-pressure turbine blades [72]. TBCs serve to insulate components from prolonged heat exposure, often reducing temperatures from 1700 K down to around 1200 K [73]. High thrust applications demand higher temperature turbines, so it is important to continue developing and understanding coatings that can more effectively mitigate heat transfer in engines. TBC systems can be constructed using various methods and materials. One such method is to use EB-PVD ZrO_2 based coatings, as they have better aerodynamic performance and strain compliance than and APS TBC [74]. The top coat, which is the layer of interest for CMAS infiltration. Figure 30 shows the

columnar microstructure of an EB-PVD coating. Melted CMAS infiltrates the inter-columnar gaps, and as the CMAS solidifies when the engine is not in use, the thermal expansion causes deformation in the TBC microstructure, which causes the desirable thermal insulation properties to degrade.

There are also two analytical approaches to modeling CMAS infiltration in a TBC, these are the open pipe and concentric pipe models [11]. The open pipe model assumes that CMAS infiltrates the inter-columnar gap with a certain permeability given by

$$k_o = \frac{(r_{eff}\phi)^2}{8\tau(1-\phi)^2}. \quad (1)$$

Here, k_0 is the permeability which relates to the ease of infiltration. Permeability is dependent on the τ, which is the tortuosity of the medium, and ϕ is the overall pore fraction of the medium. The concentric pipe model modifies the open pipe model by changing the number saying that the gaps on either side of the column are the gaps between concentric pipes. The modified permeability, k_c, is given as

$$k_c = \frac{\psi b^2}{8\tau^2}\left[1 + \frac{a^2}{b^2} + \left(1 - \frac{a^2}{b^2}\right)\frac{1}{ln\frac{a}{b}}\right] \quad (2)$$

Here, k_c is more specific to the various TBC shapes [11]. $\tau\ and\ \phi$ are the same as in the open-pipe model. The only major difference is that this model relies on a, the radius of the outer pipe, and b, the radius of the inner pipe These relationships drive the infiltration relevant to TBCs. Figure 31 shows the differences between the two pipe models. The pipe models also have their own correlations for quantities such as infiltration time [11, 75]. While these pipe models are useful for modeling overall properties of CMAS infiltration of a TBC, they fail to capture all of the kinetics, such as the infiltration effects in the feather gaps. They also fail to include any kind of

model for heat transfer, or thermal expansion. These are the shortcomings that can be assessed using simulations.

This paper proposes the use of a finite-volume method (more specifically, the Eulerian Volume-of-Fluid Model), to model the infiltration of CMAS into an idealized TBC. Previous simulation-based infiltration models have used an FEM approach [73], but this approach comes with several challenges, including difficulties with properly resolving surface tension forces. Overall the approach has potential to push the understanding of infiltration processes.

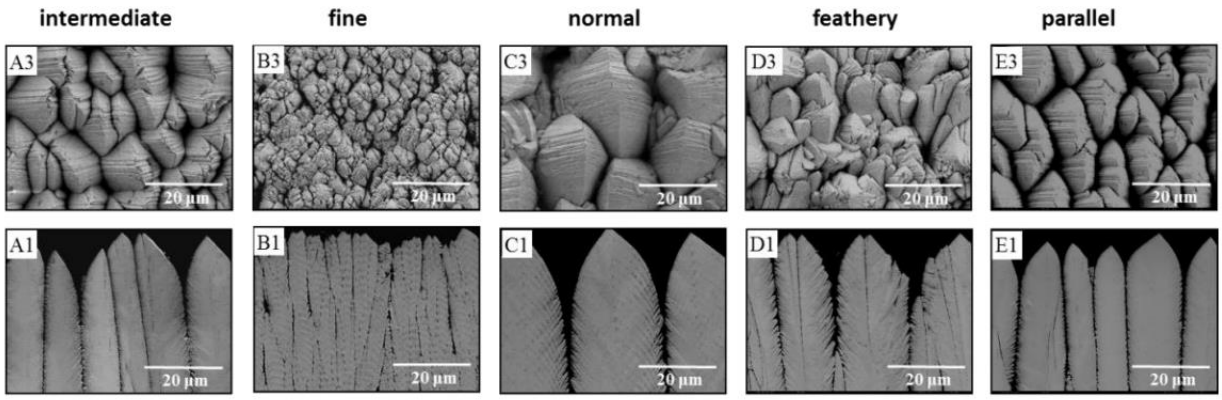

Figure 30: Various morphologies of EB-PVD TBCs under magnification [74]. The top panel depicts the TBC surface, while the lower panel shows a side view from a cut TBC.

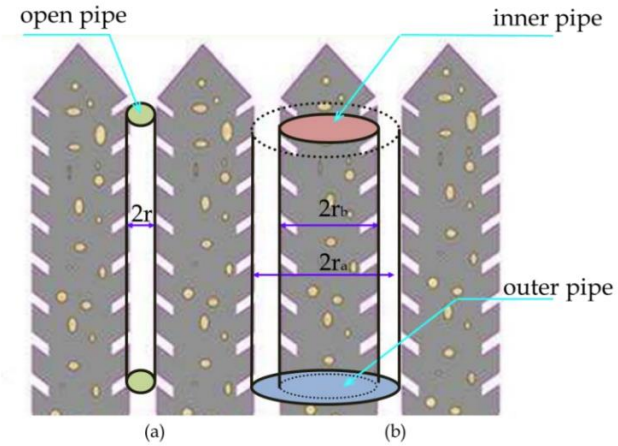

Figure 31: Comparison of open and concentric pipe models [73]

Current literature has explored several important aspects of CMAS interaction with aircraft engines. One such study includes a computational model exploring CMAS particle fan-blade interaction [55]. This study's goal was to find a distribution of particle sizes that are likely to make it past the fan stage of an aircraft engine [55].

Another important study investigated how the impact of CMAS particle size and chemical composition would affect the particle's time to equilibrate on the nozzle guide vane. The particle's properties were summarized using the thermal Stokes number. The ratio of particle impact temperature ($T_{p,imp}$) to the temperature of the fluid (T_f) was measured. The study showed that the temperature of particles with a St_{th} below unity equilibrate with the temperature of the surrounding fluid in a fraction of the surrounding fluid's response time. St_{th} larger than unity led to particles that take much longer than the surrounding fluid's response time to equilibrate with the surrounding fluid. This correlation was used as a validation methodology for this method [76].

This work seeks to do the following: 1) Give an overview of necessary background information to understand the processes involved in simulating CMAS, 2) Provide details of a

methodology in which CMAS infiltration into a TBC is directly resolved 3) Perform a design study on a parametrized TBC model to understand which dimensions lead to desirable infiltration properties, such as longer infiltration times, or less heat transfer to the TBC.

Methodology

The first step in simulating the infiltration of CMAS was to ensure the VOF method is a valid approach for capturing the melting-solidification of a CMAS particle. The methodology for validating this approach is discussed in previous work [76], and it is shown that melting particles between the solidus and liquidus temperatures of CMAS can be accurately modeled with the VOF method.

For the multiphase physics, the Eulerian Multiphase Volume-of-Fluid method was used to simulate the interactions between the two Eulerian phases, air, and CMAS. Modeling surface tension properly is critical as the infiltration is driven mostly by capillary forces. The governing equations for the VOF method in Star-CCM+ [62] are given in the context of a finite volume formulation as the conservation of mass, conservation of momentum, and conservation of energy, These equations couple to the Eulerian Multiphase VOF model and can be seen in seen in APPENDIX A: COMMONLY USED EQUATIONS.

In these equations, the subscript i denotes a particular phase, ai = Vi/V is the volume fraction of a particular phase, and S_{a_i} is a source term defined by the initialization of the phases. The VOF method implements a technique called High-Resolution Interface Capturing (HRIC). HRIC resolves the interface between the primary and secondary phases such that other properties, like surface tension and slip velocity, can be modeled as well [62]. A drawback of using the VOF method for the infiltration is the very small timesteps required to resolve the CMAS infiltration.

So, adaptive time-stepping combined with sub-iterations was used to balance computational speed and accuracy. A free-surface condition was enforced so that the Courant number $\left(\frac{u\Delta t}{\Delta x}\right)$ at the interface was around 1.0. Such a criterion is often demanded to limit the interfacial motion to only a cell.

The model was initially set up as a 2D geometry, but a 3D geometry was created later to ensure that effects attributed to the nature of 2D problems would not impede the simulation. A depiction of the mesh for the 2D geometry is provided in Figure 32. The mesh is an unstructured mesh composed of (mostly) isotropic tetrahedrals. Due to the extremely slow infiltration speeds expected, boundary layers are not expected to contribute to the overall flow physics, so no prism layers are necessary around the walls. The boundary conditions for the 2D simulation were very simple. The top of the domain is a stagnation inlet with a total pressure set to 10x the reference pressure (1 atm), and the bottom of the domain was set as a pressure outlet with a pressure much smaller than the reference pressure. The pressure difference between the inlet and outlet was set up so that a pressure gradient is maintained throughout the domain similar to experiments conducted by Naraparaju et al. [11].The sides of the domain are set as pressure outlets as well, but with a periodic interface.

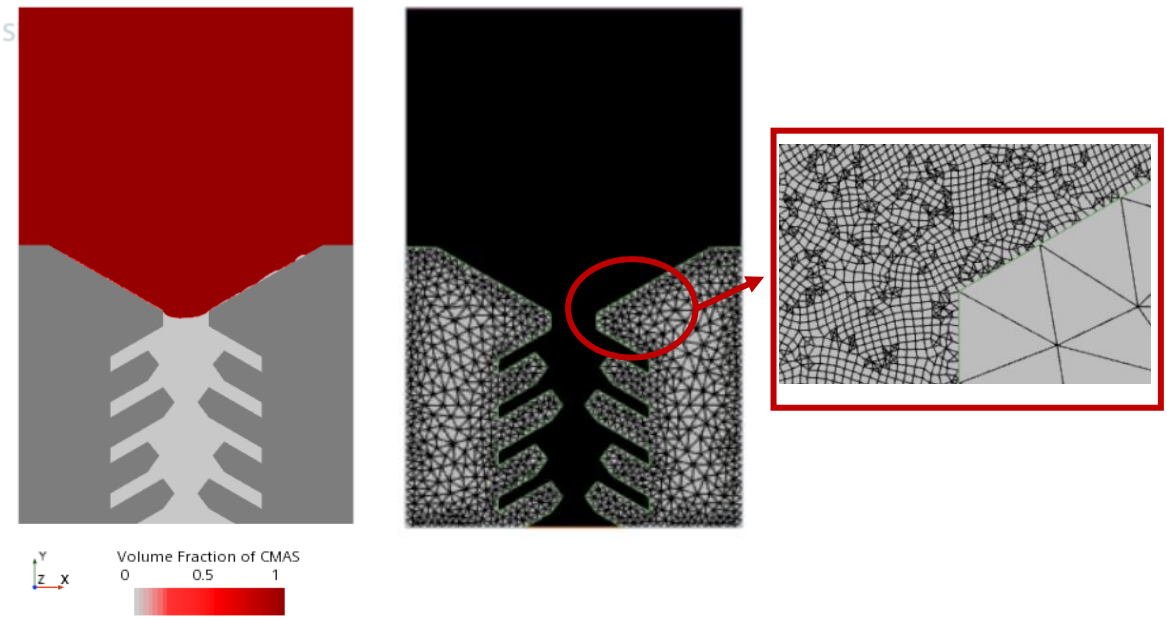

Figure 32: 2D geometry with CMAS (left), zoomed out 2D mesh , and 2D mesh zoomed in around wall region

The mesh of the 3D geometry was constructed with the same principles of the 2D mesh, however, it is generally much coarser to decrease simulation times. In 3D, it is also possible to use free-surface adaptive mesh refinement (AMR) to better resolve the CMAS-air interface. The effect of this AMR will be quantified in the results to see if it's benefit outweighs it's cost of simulation time and solution stability. The 2D geometry and mesh can be seen in Figure 32. The parametrization of the modeled TBC is summarized in Figure 33. The 3D geometry and mesh can be seen in Figure 34. The 3D boundary conditions are the same as in 2D. The wall contact angle of the CMAS phase is expected to be somewhere between 40 and 60 degrees based on experiments [11]. These values are temperature dependent though. For simplicity a constant wall contact angle of 40 degrees was chosen.

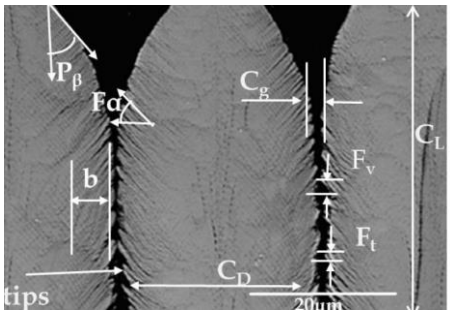

Pyramidal Angle		P_B
Feather Inclination		F_α
Feather arm thickness		F_t
Void between feathers		F_v
Length of column		C_L
Diameter of column		C_D
Length of feather arm		B
Inter-columnar gap		C_g

Figure 33: Summary of Parameterized Dimensions

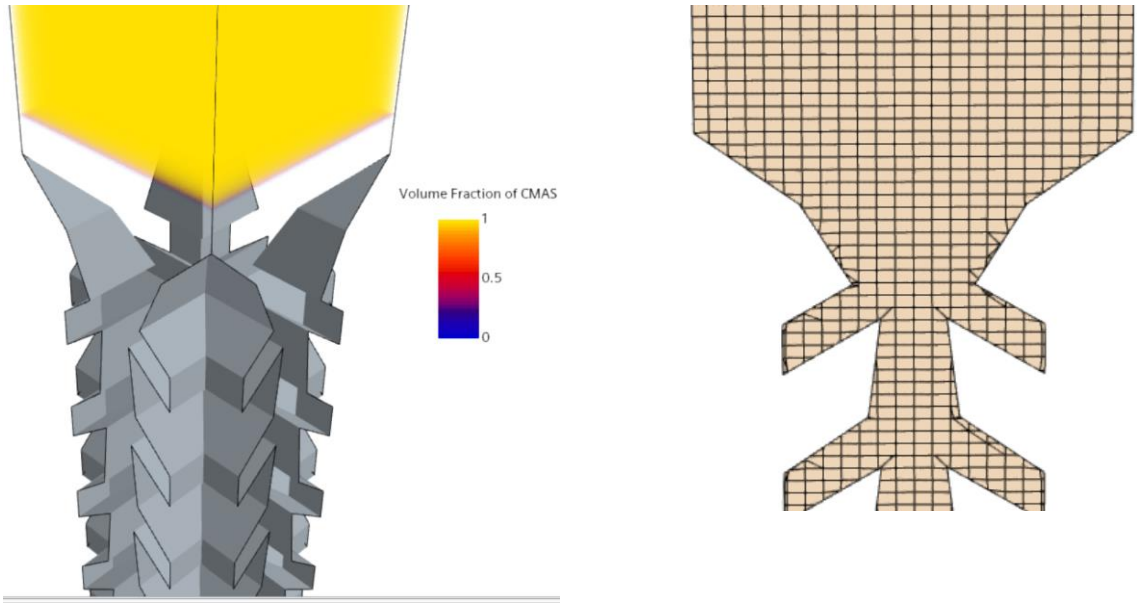

Figure 34: Isometric View of 3D geometry with CMAS (left) and 3D mesh cross-section (right)

Preliminary Results

In the 2D simulation, initial time-steps on the order of 10^{-10} s were required to satisfy the convective CFL condition. However, the adaptive time-stepping allowed the time-steps to reach an order of 10^{-7}s. The infiltration in the 2D simulation is generally stable, though slow. There are two very important issues with this 2D simulation. Firstly, the feathers receive little to no CMAS infiltration. It is known from experiments that this should not be the case. This is happening mainly because the air phase is set to a constant density, and the 2D nature of the simulation causes air to get trapped in the feather arms by the infiltrating CMAS. Once the CMAS has passed the feather gap, the air can no longer leave, so the CMAS cannot infiltrate it. This can be fixed a few different ways: 1) moving everything to a 3D geometry, 2) allowing the walls to be porous to air, allowing the air to escape through the walls and thus CMAS will infiltrate, or 3) incorporating the Ideal Gas Law. Moving forward, options 1 and 2 will be considered, as the Ideal Gas Law introduces more instabilities once enabled.

The next important issue is the overall infiltration time. The infiltration time for the *most* viscous case is supposed to be around half the time shown in Figure 35 [73]. This means that the CMAS should have reached the very last feather arm in around 500 μs. This is likely happening as a result of the capillary forces and viscous forces involved being too close to one another, making the overall infiltration slower. Steps to take to improve this would be to increase the pressure gradient. The previously mentioned step of allowing the TBC wall to be porous to air will also assist with this.

Figure 35: Infiltrating CMAS

Using what is known from this 2D simulation, new 2D and 3D simulations were created. The walls of the TBC in these simulations were allowed to be porous to air. Ideally, these new simulations will allow parametric design studies to begin.

Further characterization studies were conducted to provide insight on the sensitivity of parameters such as CMAS viscosity on the overall infiltration kinetics. Infiltration time of the experimental viscosity measurement [11], and the GRD viscosity model [10] were compared in and it was found that the experimental measurement lead to longer infiltration time, which makes sense as the experimental viscosity was generally higher over the temperature range seen in Figure 3.

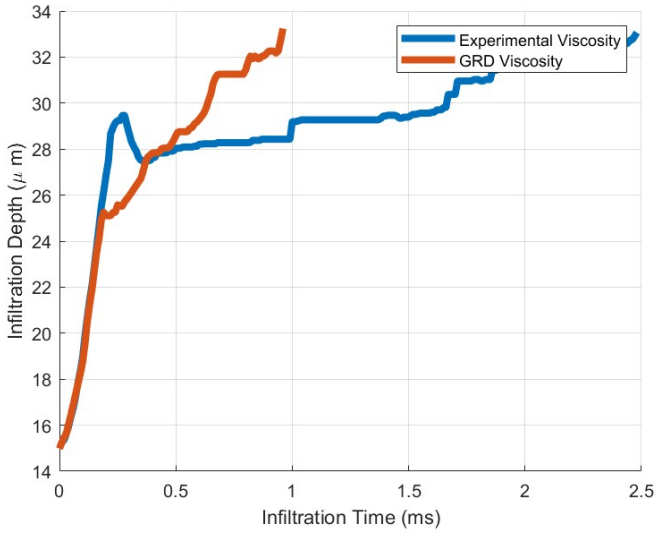

Figure 36: Infiltration Depth v. Time for the GRD Viscosity Model and the Epxerimental Viscosity Measurement

CHAPTER SEVEN: CONCLUSIONS AND FINAL REMARKS

The VOF Method for modeling, and in some cases, fully resolving multiphase flows has proven useful in several applications. Firstly, a proof of concept application was developed, directly resolving a melting CMAS particle by validating the Thermal Stokes Number against experimental data. This showed that the VOF method can be used for these directly resolved melting-solidification cases.

Next, the same method was applied to a lunar regolith particle. This time, however, the flow was coupled to a source-flow model to account for rarefied flow conditions. Also, the melting particle experienced an impact with an adiabatic wall. Results from this study showed how a partially melted lunar regolith particle can stick to surfaces, which can be problematic for lunar missions, especially when accumulation is accounted for.

Lastly, the VOF Method was used to resolve a capillary-driven flow, the infiltration of molten CMAS into a 7YSZ EB-PVD thermal barrier coating. These simulations were characterized by the infiltration depth of the CMAS as a function of time. The simulated infiltration was several orders of magnitude faster than the experimentally measured infiltration. Possible explanations include the lack of a solidification or phase change model in the simulation, or that the modeled TBC is not sufficient for accurately resolving the infiltration. Future work here includes the addition of solidification and phase change models, and performing a similar simulation on a domain consisting of a nano-CT scan of an actual TBC.

The overall success of the models developed using the VOF Method shows its robustness at handling a wide range of multiphase flows. The VOF Method is not without its faults, however. The directly resolved CMAS particle experienced stability issues at certain mesh sizes, and had a

very long run time. While the stability issues can be readily fixed by changing the mesh, the long runtime persisted through the lunar regolith and CMAS infiltration cases. Future work could involve further optimization of the SIMPLE-C algorithm to run on GPUs, allowing faster overall runtimes.

APPENDIX A: COMMONLY USED EQUATIONS

Volume Fraction Transport Equation

$$\frac{\partial}{\partial t}\int_V \alpha_i dV + \oint_A \alpha_i \boldsymbol{v} \cdot dA = \int_V \left(S_{\alpha_i} - \frac{\alpha_i}{\rho_i}\frac{D\rho_i}{Dt}\right) dV - \int_V \frac{1}{\rho_i}\nabla \cdot \left(\alpha_i \rho_i v_{d,i}\right) dV$$

VOF Continuity Equation

$$\frac{\partial}{\partial t}\int_V \rho dV + \oint_A v \cdot dA = \int_V (S) dV \ , \ S = \sum_i S_{\alpha_i}\rho_i$$

VOF Momentum Equation

$$\frac{\partial}{\partial t}\int_V \rho v dV + \oint_A \rho v \times v \cdot dA = \oint_A \rho I \cdot dA + \oint_A T \cdot dA + \int_V \rho g dV + \int_V f_b dV - \sum_i \int_A \alpha_i \rho_i v_{d,i} \times v_{d,i} dA$$

VOF Energy Equation

$$\frac{\partial}{\partial t}\int_V \rho E dV + \oint_A [\rho H v + p + \alpha_i \rho_i H_i v_{d,i}] \cdot dA = -\oint_A \dot{q}'' \cdot dA + \oint_A T \cdot v dA + \int_V S_E dV + \int_V f_b dV$$

VOF Solid Volume Fraction

$$\alpha_s^* = \begin{cases} 1 \ if \ T^* < 0 \\ f(T^*) \ if \ 0 < T^* < 1 \\ 0 \ if \ 1 < T^* \end{cases}$$

APPENDIX B: COPYRIGHT STATEMENTS

Chapter 2

Chapter 3

Chapter 4

REFERENCES

[1].Bojdo, N., and Filippone, A. "A Simple Model to Assess the Role of Dust Composition and Size on Deposition in Rotorcraft Engines," *Aerospace* Vol. 6, No. 4, 2019, p. 44.

[2].Anderson, J. D. *Computational Fluid Dynamics*: McGraw-Hill Education, 1995.

[3].Ransom, E. C. P. "Computational Methods for Fluid Dynamics, J.H. Ferziger and M. Peric, Springer-Verlag, Tiergartenstrasse 17, D-69121, Heidelberg, Germany. 1996. 356pp. Illustrated. DM74," *The Aeronautical Journal* Vol. 100, No. 998, 1996, pp. 364-364. doi: 10.1017/S0001924000067087

[4].and, M. S. I., and Gimelshein, S. F. "COMPUTATIONAL HYPERSONIC RAREFIED FLOWS," *Annual Review of Fluid Mechanics* Vol. 30, No. 1, 1998, pp. 469-505. doi: 10.1146/annurev.fluid.30.1.469

[5].Gopala, V. R., and van Wachem, B. G. M. "Volume of fluid methods for immiscible-fluid and free-surface flows," *Chemical Engineering Journal* Vol. 141, No. 1, 2008, pp. 204-221. doi: https://doi.org/10.1016/j.cej.2007.12.035

[6].Hirt, C. W., and Nichols, B. D. "Volume of fluid (VOF) method for the dynamics of free boundaries," *Journal of Computational Physics* Vol. 39, No. 1, 1981, pp. 201-225. doi: https://doi.org/10.1016/0021-9991(81)90145-5

[7].Brackbill, J. U., Kothe, D. B., and Zemach, C. "A continuum method for modeling surface tension," *Journal of Computational Physics* Vol. 100, No. 2, 1992, pp. 335-354. doi: https://doi.org/10.1016/0021-9991(92)90240-Y

[8].Li, L., Hitchman, N., and Knapp, J. "Failure of Thermal Barrier Coatings Subjected to CMAS Attack," *Journal of Thermal Spray Technology* Vol. 19, No. 1, 2010, pp. 148-155. doi: 10.1007/s11666-009-9356-8

[9].Steinberg, L., Naraparaju, R., Heckert, M., Mikulla, C., Schulz, U., and Leyens, C. "Erosion behavior of EB-PVD 7YSZ coatings under corrosion/erosion regime: Effect of TBC microstructure and the CMAS chemistry," *Journal of the European Ceramic Society* Vol. 38, No. 15, 2018, pp. 5101-5112. doi: https://doi.org/10.1016/j.jeurceramsoc.2018.06.039

[10].Giordano, D., Russell, J. K., and Dingwell, D. B. "Viscosity of magmatic liquids: A model," *Earth and Planetary Science Letters* Vol. 271, No. 1, 2008, pp. 123-134. doi: https://doi.org/10.1016/j.epsl.2008.03.038

[11].Naraparaju, R., Gomez Chavez, J. J., Niemeyer, P., Hess, K.-U., Song, W., Dingwell, D. B., Lokachari, S., Ramana, C. V., and Schulz, U. "Estimation of CMAS infiltration depth in EB-PVD TBCs: A new constraint model supported with experimental approach," *Journal of the European Ceramic Society* Vol. 39, No. 9, 2019, pp. 2936-2945. doi: https://doi.org/10.1016/j.jeurceramsoc.2019.02.040

[12].Miller, R. A. "Thermal barrier coatings for aircraft engines: history and directions," *Journal of Thermal Spray Technology* Vol. 6, No. 1, 1997, pp. 35-42. doi: 10.1007/BF02646310

[13].Mondal, K., Nuñez, L., III, Downey, C. M., and van Rooyen, I. J. "Thermal Barrier Coatings Overview: Design, Manufacturing, and Applications in High-Temperature Industries," *Industrial & Engineering Chemistry Research* Vol. 60, No. 17, 2021, pp. 6061-6077. doi: 10.1021/acs.iecr.1c00788

[14].Young, E. J., Mateeva, E., Moore, J. J., Mishra, B., and Loch, M. "Low pressure plasma spray coatings," *Thin Solid Films* Vol. 377-378, 2000, pp. 788-792. doi: https://doi.org/10.1016/S0040-6090(00)01452-8

[15].Saini, A. K., Das, D., and Pathak, M. K. "Thermal Barrier Coatings -Applications, Stability and Longevity Aspects," *Procedia Engineering* Vol. 38, 2012, pp. 3173-3179. doi: https://doi.org/10.1016/j.proeng.2012.06.368

[16].Ren, X., and Pan, W. "Mechanical properties of high-temperature-degraded yttria-stabilized zirconia," *Acta Materialia* Vol. 69, 2014, pp. 397-406. doi: https://doi.org/10.1016/j.actamat.2014.01.017

[17].Boccaccini, A. R., and Zhitomirsky, I. "Application of electrophoretic and electrolytic deposition techniques in ceramics processing," *Current Opinion in Solid State and Materials Science* Vol. 6, No. 3, 2002, pp. 251-260. doi: https://doi.org/10.1016/S1359-0286(02)00080-3

[18].Zhitomirsky, I. "Cathodic electrodeposition of ceramic and organoceramic materials. Fundamental aspects," *Advances in Colloid and Interface Science* Vol. 97, No. 1, 2002, pp. 279-317. doi: https://doi.org/10.1016/S0001-8686(01)00068-9

[19].Wakisaka, Y., Fukui, K., Kawaguchi, A., Iguma, H., Yamashita, H., Takada, N., Nishikawa, N., and Yamashita, C. "Thermo-Swing Wall Insulation Technology; - A Novel Heat Loss Reduction Approach on Engine Combustion Chamber". SAE International, 2016.

[20].Gleeson, B. "Thermal Barrier Coatings for Aeroengine Applications," *Journal of Propulsion and Power* Vol. 22, No. 2, 2006, pp. 375-383. doi: 10.2514/1.20734

[21].Sree Harsha, K. S. "Chapter 2 - Evaporation," *Principles of Vapor Deposition of Thin Films*. Elsevier, Oxford, 2006, pp. 11-143.

[22].Lee, K.-Y., Jo, S., Tan, A. J., Huang, M., Choi, D., Park, J. H., Ji, H.-I., Son, J.-W., Chang, J., Beach, G. S. D., and Woo, S. "Fast Magneto-Ionic Switching of Interface Anisotropy Using Yttria-Stabilized Zirconia Gate Oxide," *Nano Letters* Vol. 20, No. 5, 2020, pp. 3435-3441. doi: 10.1021/acs.nanolett.0c00340

[23].Koch, D., Mauer, G., and Vaßen, R. "Manufacturing of Composite Coatings by Atmospheric Plasma Spraying Using Different Feed-Stock Materials as YSZ and MoSi2," *Journal of Thermal Spray Technology* Vol. 26, No. 4, 2017, pp. 708-716. doi: 10.1007/s11666-017-0537-6

[24].Besling, W. F. A., Goossens, A., Meester, B., and Schoonman, J. "Laser-induced chemical vapor deposition of nanostructured silicon carbonitride thin films," *Journal of Applied Physics* Vol. 83, No. 1, 1998, pp. 544-553. doi: 10.1063/1.366669

[25].Bobzin, K., Bagcivan, N., Brögelmann, T., and Yildirim, B. "Influence of temperature on phase stability and thermal conductivity of single- and double-ceramic-layer EB–PVD TBC top coats consisting of 7YSZ, Gd2Zr2O7 and La2Zr2O7," *Surface and Coatings Technology* Vol. 237, 2013, pp. 56-64. doi: https://doi.org/10.1016/j.surfcoat.2013.08.013

[26].Han, J., Zou, Y., Wu, D., and Zhang, Y. "Investigating the thermal, mechanical and thermal cyclic properties of plasma-sprayed Al2O3-7YSZ/7YSZ double ceramic layer TBCs," *Journal of the European Ceramic Society* Vol. 43, No. 9, 2023, pp. 4124-4135. doi: https://doi.org/10.1016/j.jeurceramsoc.2023.03.004

[27].Ye, D., Wang, W., Huang, J., Lu, X., and Zhou, H. "Nondestructive Interface Morphology Characterization of Thermal Barrier Coatings Using Terahertz Time-Domain Spectroscopy," *Coatings* Vol. 9, No. 2, 2019, p. 89.

[28].Chen, C. C., Lee, D. J., Pollock, T., and Whitaker, J. F. "Terahertz characterization of interfacial oxide layers and voids for health monitoring of ceramic coatings" *2009 34th International Conference on Infrared, Millimeter, and Terahertz Waves*. 2009, pp. 1-2.

[29].Ogawa, K., Minkov, D., Shoji, T., Sato, M., and Hashimoto, H. "NDE of degradation of thermal barrier coating by means of impedance spectroscopy," *NDT & E International* Vol. 32, No. 3, 1999, pp. 177-185. doi: https://doi.org/10.1016/S0963-8695(98)00069-3

[30].Chen, H.-L. R., Zhang, B., Alvin, M. A., and Lin, Y. "Ultrasonic Detection of Delamination and Material Characterization of Thermal Barrier Coatings," *Journal of Thermal Spray Technology* Vol. 21, No. 6, 2012, pp. 1184-1194. doi: 10.1007/s11666-012-9811-9

[31].Eldridge, J. I., and Bencic, T. J. "Monitoring delamination of plasma-sprayed thermal barrier coatings by reflectance-enhanced luminescence," *Surface and Coatings Technology* Vol. 201, No. 7, 2006, pp. 3926-3930. doi: https://doi.org/10.1016/j.surfcoat.2006.08.008

[32].Moskal, G., Swadźba, R., and Witala, B. "Non-destructive measurement of top coat thickness in TBC systems by 3D optical topometry," *Nondestructive Testing and Evaluation* Vol. 30, No. 1, 2015, pp. 39-48. doi: 10.1080/10589759.2014.984297

[33].Taqi, A. H., Faraj, K. A., and Zaynal, S. A. "The Effect of Long-Term X-Ray Exposure on Human Lymphocyte," *Journal of Biomedical Physics and Engineering* Vol. 9, No. 1, 2019, pp. 127-132. doi: 10.31661/jbpe.v0i0.935

[34].Davies, G., and Linfield, E. "Bridging the terahertz gap," *Physics World* Vol. 17, No. 4, 2004, p. 37. doi: 10.1088/2058-7058/17/4/34

[35].Ali, M. S., Song, S., and Xiao, P. "Degradation of thermal barrier coatings due to thermal cycling up to 1150°C," *Journal of Materials Science* Vol. 37, No. 10, 2002, pp. 2097-2102. doi: 10.1023/A:1015245920054

[36].Keyvani, A., Saremi, M., and Sohi, M. H. "Oxidation resistance of YSZ-alumina composites compared to normal YSZ TBC coatings at 1100°C," *Journal of Alloys and Compounds* Vol. 509, No. 33, 2011, pp. 8370-8377. doi: https://doi.org/10.1016/j.jallcom.2011.05.029

[37].Peng, H., Wang, L., Guo, L., Miao, W., Guo, H., and Gong, S. "Degradation of EB-PVD thermal barrier coatings caused by CMAS deposits," *Progress in Natural Science: Materials International* Vol. 22, No. 5, 2012, pp. 461-467. doi: https://doi.org/10.1016/j.pnsc.2012.06.007

[38].Borom, M. P., Johnson, C. A., and Peluso, L. A. "Role of Environmental Deposits in Spallation of Thermal Barrier Coatings on Aeroengine and Land-Based Gas Turbine Hardware" *ASME 1996 International Gas Turbine and Aeroengine Congress and Exhibition*. Vol. Volume 5: Manufacturing Materials and Metallurgy; Ceramics; Structures and Dynamics; Controls, Diagnostics and Instrumentation; Education; General, 1996.

[39].Borom, M. P., Johnson, C. A., and Peluso, L. A. "Role of environment deposits and operating surface temperature in spallation of air plasma sprayed thermal barrier coatings," *Surface and Coatings Technology* Vol. 86-87, 1996, pp. 116-126. doi: https://doi.org/10.1016/S0257-8972(96)02994-5

[40].Boyce, M. P. "2 - Advanced industrial gas turbines for power generation," *Combined Cycle Systems for Near-Zero Emission Power Generation*. Woodhead Publishing, 2012, pp. 44-102.

[41].Krämer, S., Yang, J., Levi, C. G., and Johnson, C. A. "Thermochemical Interaction of Thermal Barrier Coatings with Molten CaO–MgO–Al2O3–SiO2 (CMAS) Deposits," *Journal of the American Ceramic Society* Vol. 89, No. 10, 2006, pp. 3167-3175. doi: https://doi.org/10.1111/j.1551-2916.2006.01209.x

[42].Wellman, R., Whitman, G., and Nicholls, J. R. "CMAS corrosion of EB PVD TBCs: Identifying the minimum level to initiate damage," *International Journal of Refractory Metals and Hard Materials* Vol. 28, No. 1, 2010, pp. 124-132. doi: https://doi.org/10.1016/j.ijrmhm.2009.07.005

[43].Naraparaju, R., Schulz, U., Mechnich, P., Döbber, P., and Seidel, F. "Degradation study of 7wt.% yttria stabilised zirconia (7YSZ) thermal barrier coatings on aero-engine combustion chamber parts due to infiltration by different CaO–MgO–Al2O3–SiO2 variants," *Surface and Coatings Technology* Vol. 260, 2014, pp. 73-81. doi: https://doi.org/10.1016/j.surfcoat.2014.08.079

[44].Costa, G., Harder, B. J., Wiesner, V. L., Zhu, D., Bansal, N., Lee, K. N., Jacobson, N. S., Kapush, D., Ushakov, S. V., and Navrotsky, A. "Thermodynamics of reaction between gas-turbine ceramic coatings and ingested CMAS corrodents," *Journal of the American Ceramic Society* Vol. 102, No. 5, 2019, pp. 2948-2964. doi: https://doi.org/10.1111/jace.16113

[45].Xia, J., Yang, L., Wu, R. T., Zhou, Y. C., Zhang, L., Huo, K. L., and Gan, M. "Degradation mechanisms of air plasma sprayed free-standing yttria-stabilized zirconia thermal barrier coatings exposed to volcanic ash," *Applied Surface Science* Vol. 481, 2019, pp. 860-871. doi: https://doi.org/10.1016/j.apsusc.2019.03.084

[46].Mechnich, P., and Braue, W. "Solid-State CMAS Corrosion of an EB-PVD YSZ Coated Turbine Blade: Zr4+ Partitioning and Phase Evolution," *Journal of the American Ceramic Society* Vol. 98, No. 1, 2015, pp. 296-302. doi: https://doi.org/10.1111/jace.13241

[47].Morelli, S., Testa, V., Bolelli, G., Ligabue, O., Molinari, E., Antolotti, N., and Lusvarghi, L. "CMAS corrosion of YSZ thermal barrier coatings obtained by different thermal spray processes," *Journal of the European Ceramic Society* Vol. 40, No. 12, 2020, pp. 4084-4100. doi: https://doi.org/10.1016/j.jeurceramsoc.2020.04.058

[48].Brindley, W. J., and Leonhardt, T. A. "Metallographic techniques for evaluation of thermal barrier coatings," *Materials Characterization* Vol. 24, No. 2, 1990, pp. 93-101. doi: https://doi.org/10.1016/1044-5803(90)90029-J

[49].Rose, A., Gomez Chavez, J. J., Mechnich, P., Kelm, K., Schulz, U., and Naraparaju, R. "Novel magnetron sputtered yttrium-silicon-iron oxide as CMAS resistant top coat material for environmental barrier coatings," *Corrosion Science* Vol. 215, 2023, p. 111053. doi: https://doi.org/10.1016/j.corsci.2023.111053

[50].Liu, Y. Z., Zheng, S. J., Zhu, Y. L., Wei, H., and Ma, X. L. "Microstructural evolution at interfaces of thermal barrier coatings during isothermal oxidation," *Journal of the European Ceramic Society* Vol. 36, No. 7, 2016, pp. 1765-1774. doi: https://doi.org/10.1016/j.jeurceramsoc.2016.02.011

[51].Chen, W., and Zhao, L. "Review – Volcanic Ash and its Influence on Aircraft Engine Components," *Procedia Engineering* Vol. 99, 2015, pp. 795-803. doi: 10.1016/j.proeng.2014.12.604

[52]."MITIGATING THE IMPACT OF VOLCANIC ASH CLOUDS ON AVIATION—WHAT DO WE NEED TO KNOW?" *U.S. House of Representatives Committee on Science, Space, & Technology*. 2318 Rayburn House Office Building, 2010.

[53].Pilch, M., and Erdman, C. A. "Use of breakup time data and velocity history data to predict the maximum size of stable fragments for acceleration-induced breakup of a liquid drop," *International Journal of Multiphase Flow* Vol. 13, No. 6, 1987, pp. 741-757. doi: https://doi.org/10.1016/0301-9322(87)90063-2

[54].Cao, Y., and Xin, M. "Numerical Simulation of Supercooled Large Droplet Icing Phenomenon: A Review," *Archives of Computational Methods in Engineering* Vol. 27, No. 4, 2020, pp. 1231-1265. doi: 10.1007/s11831-019-09349-5

[55].Vogel, A., Durant, A., Cassiani, M., Clarkson, R., Slaby, M., Diplas, S., Krüger, K., and Stohl, A. "Simulation of Volcanic Ash Ingestion Into a Large Aero Engine: Particle–Fan Interactions," *Journal of Turbomachinery* Vol. 141, 2018. doi: 10.1115/1.4041464

[56].Ganti, H., Khare, P., and Bravo, L. "Binary collision of CMAS droplets—Part I: Equal-sized droplets," *Journal of Materials Research* Vol. 35, No. 17, 2020, pp. 2260-2274. doi: 10.1557/jmr.2020.138

[57].Bean, A. L. "NASA SP-235". 1970.

[58].R, G. "Apollo 17 Mission Report". 1973.

[59].Nanson Iii, R. A. "Navier/Stokes/Direct Simulation Monte Carlo Modeling of Small Cold Gas Thruster Nozzle and Plume Flows". Worcester Polytechnic Institute, 2002.

[60].Bird, G. A. *Molecular gas dynamics and the direct simulation of gas flows*. Oxford; New York: Clarendon Press ; Oxford University Press, 1994.

[61].White, C., Matthew K. Borg, Thomas J. Scanlon, Stephen M. Longshaw, Benzi John, David R. Emerson, and Jason M. Reese. "dsmcFoam+: An OpenFOAM based direct simulation Monte Carlo solver," *omputer Physics Communications* Vol. 224, 2018, pp. 22-43.

[62].Star-ccm+. "Siemens PLM Software". Munich, Germany, Ver. 17.02.004.

[63].Carrier, W. D. "Particle Size Distribution of Lunar Soil," *Journal of Geotechnical and Geoenvironmental Engineering* Vol. 129, No. 10, 2003, pp. 956-959. doi: doi:10.1061/(ASCE)1090-0241(2003)129:10(956)

[64].Yeager, T. R., Fontes, D. H., Metzger, P., and Kinzel, M. P. "Numerical Model of Jet Impingement and Particle Trajectories in Extraterrestrial Landing Events Using an Euler-Lagrange Method," *AIAA Scitech 2020 Forum*. 2020.

[65].Fontes, D., Mantovani, J. G., and Metzger, P. "Numerical estimations of lunar regolith trajectories and damage potential due to rocket plumes," *Acta Astronautica* Vol. 195, 2022, pp. 169-182. doi: https://doi.org/10.1016/j.actaastro.2022.02.016

[66].Lane, J. E., Metzger, P. T., Immer, C. D., and Li, X. "Lagrangian Trajectory Modeling of Lunar Dust Particles," *Earth & Space 2008*. 2008, pp. 1-9.

[67].Lumpkin, F. E., Fitzgerald, S. M., LeBeau, G. J., Aeronautics, A. I. o., and Astronautics. *Study of 3D Rarefied Flow on a Flat Plate in the Wake of a Cylinder*: AIAA, 1999.

[68].Colozza, A. "Analysis of lunar regolith thermal energy storage," 1991.

[69].J. K. Mitchell, W. N. H., R.F. Scott, N. C. Costes, W.D. Carrier III, L. G. Bromwell. "Mechanical Properties of Lunar Soil: Density, Porosity, Cohesion, and Angle of Internal Friction" *Third Lunar Science Conference*. Vol. 3, The M.I.T. Press, 1972, pp. 3235-3253.

[70].Altun, A. A., Ertl, F., Marechal, M., Makaya, A., Sgambati, A., and Schwentenwein, M. "Additive manufacturing of lunar regolith structures," *Open Ceramics* Vol. 5, 2021, p. 100058. doi: https://doi.org/10.1016/j.oceram.2021.100058

[71].III, J. L. S. F. A. A. R. G. G. *International SAMPE Metals Conference*. 1992.

[72].Bennett, T. D., and Yu, F. "A nondestructive technique for determining thermal properties of thermal barrier coatings," *Journal of Applied Physics* Vol. 97, No. 1, 2005, p. 013520. doi: 10.1063/1.1826217

[73].Sirigiri, A. K. "Modeling and simulation of CMAS infiltration in EB-PVD TBCs" *Institute of Materials Research*. University of Duisburg-Essen, DLR, Cologne, Germany, 2018.

[74].Flores Renteria, A. W. A. K. "A small-angle scattering analysis of the influence of manufacture and thermal induced morpological changes on the thermal conductivity of EB-PVD PYSZ thermal barrier coatings," *Fakultät für Georessourcen und Materialtechnik*, 2007.

[75].Naraparaju, R., Hüttermann, M., Schulz, U., and Mechnich, P. "Tailoring the EB-PVD columnar microstructure to mitigate the infiltration of CMAS in 7YSZ thermal barrier coatings," *Journal of the European Ceramic Society* Vol. 37, No. 1, 2017, pp. 261-270. doi: https://doi.org/10.1016/j.jeurceramsoc.2016.07.027

[76].Cavainolo, B., and Kinzel, M. "Investigation of Volume-of-Fluid Method to Simulate Melting-Solidification of CMAS Particles" *ASME 2022 Fluids Engineering Division Summer Meeting*. Vol. Volume 2: Multiphase Flow (MFTC); Computational Fluid Dynamics (CFDTC); Micro and Nano Fluid Dynamics (MNFDTC), 2022.